

PARSEC V2.0: Stellar tracks and isochrones of low and intermediate mass stars with rotation

C. T. Nguyen^{1,3}, G. Costa^{2,3,4}, L. Girardi³, G. Volpato², A. Bressan¹, Y. Chen^{5,6}, P. Marigo², X. Fu^{1,7,8}, and P. Goudfrooij⁹

¹ SISSA, Via Bonomea 265, I-34136 Trieste, Italy,
e-mail: cnghuyen@sissa.it

² Dipartimento di Fisica e Astronomia, Università degli studi di Padova, Vicolo Osservatorio 3, Padova, Italy,
e-mail: guglielmo.costa@unipd.it

³ INAF Osservatorio Astronomico di Padova, Vicolo dell'Osservatorio n. 5, Padova, Italy

⁴ INFN - Padova, Via Marzolo 8, I-35131, Padova, Italy

⁵ Anhui University, Hefei 230601, China

⁶ National Astronomical Observatories, Chinese Academy of Sciences, Beijing 100101, China

⁷ Purple Mountain Observatory, Chinese Academy of Sciences, Nanjing 210023, China

⁸ INAF Osservatorio di Astrofisica e Fisica dello Spazio, via Gobetti 93/3, 40129 Bologna, Italy

⁹ Space Telescope Science Institute, 3700 San Martin Drive, Baltimore, MD 21218, USA

ABSTRACT

We present a new comprehensive collection of stellar evolutionary tracks and isochrones for rotating low- and intermediate-mass stars assembled with the updated version of PARSEC V2.0. This version includes our recent calibration of the extra mixing from overshooting and rotation, as well as several improvements in nuclear reaction network, treatment of convective zones, mass loss and other physical input parameters. The initial mass of the stellar models covers the range from $0.09 M_{\odot}$ to $14 M_{\odot}$, for six sets of initial metallicity, from $Z=0.004$ to $Z=0.017$. Rotation is considered for stars above $\sim 1 M_{\odot}$ with a smooth transition between non-rotating and extremely fast-rotating models, based on the initial mass. For stars more massive than $\sim 1.3 M_{\odot}$ the full rotation range, from low to the critical one, is considered. We adopt the solar-scaled chemical mixtures with $Z_{\odot} = 0.01524$. All the evolutionary phases from the pre-main-sequence to the first few thermal-pulses on the asymptotic-giant-branch or central C exhaustion, are considered. The corresponding theoretical isochrones are further derived with TRILEGAL code and are converted in several photometric systems, taking into account different inclination angles. Besides magnitudes, they also offer many other stellar observables in line with the data that are being provided by current large surveys. The new collection is fully integrated in a user friendly WEB interface for the benefit of easily performing stellar population studies.

Key words. Stars: evolution - Stars: rotation - Stars: Hertzsprung-Russell and C-M diagrams - Stars: low-mass.

1. Introduction

The PAdova and tRIeste Stellar Evolutionary Code, PARSEC, was first implemented in Bressan et al. (2012), and then used in several works aimed to produce large grids of stellar evolutionary tracks and isochrones. For instance, Chen et al. (2014) extended the calculation to very low-mass star models, Tang et al. (2014) and Chen et al. (2015) pursued massive stars up to $350 M_{\odot}$, and Fu et al. (2018) studied the evolution with α -enhanced compositions. Extended sets of isochrones using PARSEC tracks were described in Bressan et al. (2012) and Marigo et al. (2017). More recently, a significant development was presented in Costa et al. (2019b), who included the effects of rotation in the new version of the code PARSEC V2.0¹.

As described in von Zeipel (1924a,b); Kippenhahn et al. (1970); Zahn (1992); Meynet & Maeder (1997); Chieffi & Limongi (2013b, 2017) rotation might have a significant im-

pact on the stellar structure induced by both geometrical distortion, extra-mixing, and enhanced mass loss rates. Observational evidence on the large fractions of rapidly rotating stars among the Milky Way field stars (e.g. Royer et al. 2007) and in star clusters in Magellanic Clouds (e.g. Dupree et al. 2017; D'Antona et al. 2017), suggests that rotation may indeed become an important driving agent for stellar evolution. Furthermore, it may be concurrent with other physical processes which drive extra-mixing, such as the convective overshooting (see e.g. Jermyn et al. 2018; Costa et al. 2019b). The effect of extra mixing caused by overshooting from the unstable core has been introduced a few decades ago (e.g. Saslaw & Schwarzschild 1965; Maeder 1975; Roxburgh 1978; Bressan et al. 1981, 1986; Bertelli et al. 1984, 1990a; Bressan et al. 1993; Meynet et al. 1994; Fagotto et al. 1994a,b; Girardi et al. 2000a), and is now incorporated in most libraries of stellar evolutionary tracks (e.g. Demarque et al. 2004; Pietrinferni et al. 2004; Weiss & Schlattl 2008; Paxton et al. 2011, 2018; Mowlavi et al. 2012; Bressan et al. 2012; Bossini et al. 2015; Spada et al. 2017; Hidalgo et al. 2018). Many authors also suggest a varia-

¹ Stellar tracks and isochrones computed in this work are available at the following links: <http://stev.oapd.inaf.it/PARSEC>, and <http://stev.oapd.inaf.it/cmd>, respectively.

tion of the overshooting efficiency, usually parameterized by the efficiency parameter λ_{ov} , with the initial mass (see e.g. Pols et al. 1998). Analysis of double-lined eclipsing binaries (DLEBs; Claret & Torres 2016, 2017, 2018, 2019) supports a growing efficiency in the mass range between $\sim 1 - 1.7 M_{\odot}$ with a plateau in λ_{ov} above this mass range. However, the best fits of the DLEBs parameters require a certain degree of stochasticity in some other important parameters, such as the mixing length scale, which in our opinion is difficult to accept, particularly in the case of binary components with the same mass. Indeed, Costa et al. (2019b) showed that the observations of DLEBs could be well explained with the interplay between a *fixed* overshooting efficiency and a varying initial rotational velocity. In fact, the latter also depends on environmental conditions. The results obtained by Costa et al. (2019b), can thus be considered as an important step in the calibration of the efficiency of the overshooting phenomenon, at least in the domain of low- and intermediate-mass stars. This calibration has been subsequently supported by a combined analysis of Cepheids in the LMC star cluster NGC1866 and the color-magnitude diagrams (CMDs) of its multiple stellar populations (Costa et al. 2019a).

After these initial tests performed with the new code, we here present in this paper the new sets of evolutionary tracks and the corresponding isochrones for the PARSEC models with rotation. The initial mass range presented in this paper goes from $0.09 M_{\odot}$ to $14 M_{\odot}$. Models of more massive stars have already been computed for some particular purposes (Spera et al. 2019; Costa et al. 2021, 2022) but the full set including rotation is still in preparation and will be presented in a dedicated paper.

All the tracks start at the pre-main-sequence (PMS) phase and are terminated at a stage that depends on the initial mass: either at ages largely exceeding the Hubble time, or at the initial stages of thermally-pulsing asymptotic giant branch, or at carbon exhaustion for more massive stars. The tracks are computed with an initial metal content ranging from $Z = 0.004$ to 0.017 , and with an initial He mass fraction following a linear enrichment law (Bressan et al. 2012). Tracks at lower metallicity are being computed with an enhanced partition, the details of these models with rotation will be presented in the coming project. For every metallicity, we consider the initial rotation rates from zero to the critical value. The theoretical isochrones are then derived and converted into several photometric systems.

The structure of this paper is as follows. In Sect. 2 we review the main input physics used in the present calculations. We will pay particular attention to differences with respect to the previous non-rotating models, in the case of important changes of physical input. In Sect. 3 we describe the effects of rotational mixing on the evolution of our stellar models. In this section, we also compare our current models with previous non-rotating ones. We also perform some comparison with some existing models in the literature. The corresponding isochrones and the quantities provided are described in detail in Sect. 4. Finally, in Sect. 5, we show a few preliminary fits to the observed CMDs of the two open clusters M67 and NGC 6633, and draw our main conclusions.

2. Input physics

The input physics used in PARSEC is described in Bressan et al. (2012); Tang et al. (2014); Chen et al. (2014); Fu et al. (2018) and Costa et al. (2019b,a). Here, we briefly summarise the main points that are more important for the low- and intermediate-mass stars dealt with in this paper.

2.1. Solar metallicity, opacities, nuclear reactions, mixing length, equation of state

The abundance of elements heavier than ${}^4\text{He}$ in the Sun is still uncertain. The early compilation by Grevesse & Sauval (1998), consisting of the abundances of 90 elements from lithium to uranium, yielded the solar metallicity $Z_{\odot} = 0.017$. Later, Asplund et al. (2006, 2009) claimed lower values, $Z_{\odot} = 0.0122$ and $Z_{\odot} = 0.0134$, respectively, or Lodders et al. (2009) with $Z_{\odot} = 0.0141$. Recent solar wind measurements give $Z_{\odot} = 0.0196 \pm 0.0014$ (von Steiger & Zurbuchen 2016). In this paper, we adopt the solar-scaled mixtures by Caffau et al. (2011) where the current solar metallicity is $Z_{\odot} = 0.01524$, which is an intermediate value between those preferred by Asplund et al. (2009) and von Steiger & Zurbuchen (2016). Further extensions to other metallicity ranges with more suitable input physics, e.g. α -enhanced mixtures will be provided in the forthcoming works.

The Rosseland mean opacities, κ_{rad} , are the same as those of PARSEC V1.2S. In the high temperature regime, $4.2 \leq \log(T/K) \leq 8.7$, the opacity tables are provided by the Opacity Project At Livermore (OPAL; see Iglesias & Rogers 1996), while in the low temperature regime $3.2 \leq \log(T/K) \leq 4.1$ we generate the opacity tables with the AESOPUS tool (see Marigo & Aringer 2009, for details). In the transition region $4.1 \leq \log(T/K) \leq 4.2$, the opacities are linearly interpolated between the OPAL and AESOPUS values. The contribution from conduction is computed following Itoh et al. (2008).

The transport of convective energy is described by the mixing length theory of Böhm (1958), adopting the value of mixing-length parameter $\alpha_{\text{MLT}} = 1.74$ calibrated on the solar model by Bressan et al. (2012) (see also Sonoi et al. 2019 for more calibrations). It is interesting, however, to note that the variation of α_{MLT} for different stars has been recently called out, e.g. Viani et al. (2018) suggests a dependency of $\alpha_{\text{MLT}}/\alpha_{\text{MLT}\odot}$ on gravity, effective temperature and metallicity, while the study of Song et al. (2020) in FGK stars mainly focuses on the impact from metallicity. While these recent studies might be an inspiration for future works, at the moment we use the solar mixing-length parameter for all calculations, $\alpha_{\text{MLT}} = \alpha_{\text{MLT}\odot} = 1.74$.

The equation of state in PARSEC V2.0 is computed with the freely available FREEEOS code developed by A.W. Irwin².

The nuclear reaction network, after the updates by Fu et al. (2018) and by Costa et al. (2021), includes the p-p chains, the CNO tri-cycle, the Ne-Na and Mg-Al chains, ${}^{12}\text{C}$, ${}^{16}\text{O}$ and ${}^{20}\text{Ne}$ burning reactions, and the α -capture reactions up to ${}^{56}\text{Ni}$, for a total of 72 different reactions tracing 32 isotopes: ${}^1\text{H}$, D , ${}^3\text{He}$, ${}^4\text{He}$, ${}^7\text{Li}$, ${}^7\text{Be}$, ${}^{12}\text{C}$, ${}^{13}\text{C}$, ${}^{14}\text{N}$, ${}^{15}\text{N}$, ${}^{16}\text{O}$, ${}^{17}\text{O}$, ${}^{18}\text{O}$, ${}^{19}\text{F}$, ${}^{20}\text{Ne}$, ${}^{21}\text{Ne}$, ${}^{22}\text{Ne}$, ${}^{23}\text{Na}$, ${}^{24}\text{Mg}$, ${}^{25}\text{Mg}$, ${}^{26}\text{Mg}$, ${}^{26}\text{Al}$, ${}^{27}\text{Al}$, ${}^{28}\text{Si}$, ${}^{32}\text{S}$, ${}^{36}\text{Ar}$, ${}^{40}\text{Ca}$, ${}^{44}\text{Ti}$, ${}^{48}\text{Cr}$, ${}^{52}\text{Fe}$, ${}^{56}\text{Ni}$, ${}^{60}\text{Zn}$. We note that in the present calculations

² <http://freeeos.sourceforge.net/>

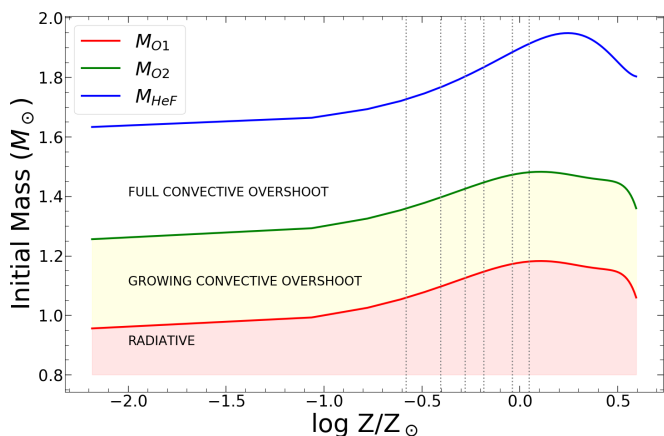


Fig. 1: The transition masses (M_{O1} , M_{O2} , M_{HeF}) as function of metallicity in the case of no rotation. The red and green lines indicate M_{O1} and M_{O2} , respectively; The blue line indicates M_{HeF} . The red area indicates models with a radiative core without convective overshooting. The yellow area delineates the region of growing overshooting efficiency, while full overshooting efficiency occurs in the region above the green line. The vertical dotted-grey lines places at the six computed initial metallicities. The solar metallicity is $Z_{\odot} = 0.01524$ from Caffau et al. (2011).

we do not go beyond the central carbon burning (but see Costa et al. 2021, for massive stars).

2.2. Convective Overshooting

Core overshooting (COV): The convective unstable region is well defined within the framework of the Schwarzschild criterion (Schwarzschild 1958). However, in reality, the convective elements can travel up to a certain point beyond the border of the unstable region until their velocity drops to zero. This phenomenon is called overshooting. The determination of the edge of the true convective core was described in Bressan et al. (1981). In PARSEC, the overshooting parameter (λ_{ov}) is taken across the unstable border; therefore, the core overshooting length is $l_{ov} \sim \frac{1}{2}\lambda_{ov}H_P$, where H_P is the local pressure scale height.

Envelope overshooting (EOV): The overshooting downward from the base of the convective envelope has been invoked to explain the observations of the location of the Red-Giant-Branch bump (RGBB) or the extension of blue loops in the CMD (Alongi et al. 1991; Cassisi et al. 2002; Tang et al. 2014; Fu et al. 2018). Solar calibration with helioseismic data have been done by Christensen-Dalsgaard et al. (2011).

In PARSEC models, the treatment of overshoot from both the convective core and envelope are related to the initial masses. For this reason, we will describe better the values of overshooting parameters that we use in our calculations in the next subsection.

2.3. Mass Range for Core and Envelope Overshooting

In a narrow interval of masses around $1 M_{\odot}$, there is the transition between stars that burn central hydrogen in a radiative core and those that burn hydrogen in a convective

core due to the predominance of the CNO-cycle over the pp-cycle. Assessing the efficiency of core overshooting in this mass range is a particularly delicate matter both theoretically (e.g Bertelli et al. 1986, 1990b; Aparicio et al. 1990; Ventura et al. 1998; Mowlavi et al. 2012; Higl et al. 2021) and observationally (e.g. Torres et al. 2014; Claret & Torres 2016, 2018; Noll et al. 2021). This happens because the inclusion of overshooting modifies the structure and the following evolution of the stars in an irreversible way. In fact, the smallest stars in this mass range reach the zero-age main sequence with small convective cores that disappear as the central H-burning proceeds. If we apply an efficient overshooting to these models, the convective cores do not disappear, but instead tend to become larger and larger, producing a significantly different evolution. To avoid this behaviour that is not favoured by observations (Costa et al. 2019b; Girardi et al. 2000b), we define the limiting mass M_{O1} as the largest initial mass of a star showing a vanishing convective core during the early hydrogen burning phase, calculated without overshooting. This mass depends on the initial chemical composition adopted. On the other hand, slightly above this mass limit, observations favour an already well-developed overshooting efficiency, with $\lambda_{ov} = \lambda_{ov,max}$. This second mass limit is defined as $M_{O2} = M_{O1} + 0.3M_{\odot}$.

In PARSEC V2.0, we define an initial mass range where the transition from models with a radiative core to models with a fully-grown convective core takes place, $M_{O1} \leq M_i \leq M_{O2}$. For initial masses M_i below M_{O1} , the core is stable against convection and energy is transported by radiation. For M_i between M_{O1} and M_{O2} , the overshooting parameter is let to increase linearly from $\lambda_{ov} = 0$ up to a maximum value $\lambda_{ov,max}$, in order to have a smooth transition in the properties of the stars. For $M_i \geq M_{O2}$, the overshoot is applied with its maximum efficiency, $\lambda_{ov} = \lambda_{ov,max} = 0.4$ following Costa et al. (2019b). This value corresponds to an overshooting length, l_{ov} , which extends about $0.2 H_P$ above the Schwarzschild border.

In this paper, we decided to switch on the EOV for low- and intermediate-mass stars only. For stars with mass $M_i < M_{O1}$ we adopted $\Lambda_e = 0.5 H_P$ as inspired by Fu et al. (2018); for stars with mass $M_i > M_{O2}$ we applied the maximum efficiency as we did for COV, therefore $\Lambda_e = 0.7 H_P$ as pointed out in Alongi et al. (1991) and Bressan et al. (2012). In the transition region, Λ_e of a star is linearly interpolated between $0.5 H_P$ and $0.7 H_P$. Table 1 shows the values of λ_{ov} and Λ_e adopted for each initial mass.

2.4. Rotation

We use PARSEC V2.0 to compute evolutionary tracks of rotating low- and intermediate-mass stars. The code uses the methodology developed by Kippenhahn & Thomas (1970) and Meynet & Maeder (1997), implemented and described in Costa et al. (2019b,a). The basic quantity describing the effect of rotation in the stellar structure is the angular rotation rate, ω , defined as

$$\omega = \frac{\Omega}{\Omega_c}, \quad \Omega_c = \left(\frac{2}{3}\right)^{3/2} \sqrt{\frac{GM}{R_{pol}^3}}. \quad (1)$$

where Ω is the angular velocity, Ω_c is the critical angular velocity (or break-up velocity), that is, the angular velocity at which the centrifugal force is equal to the effective gravity

at the equator. G is the gravitational constant, M is the mass enclosed by R_{pol} that is the polar radius.

We consider a wide range of initial rotation rates, from non-rotating models ($\omega_i = 0$), to models initially very near the critical break-up rotational velocity ($\omega_i = 0.99$).

It is commonly accepted that low-mass stars do not reach high values of the rotational speed, compared to intermediate and high-mass stars. McQuillan et al. (2014) reports a sample of the rotation period of more than 34,000 main-sequence (MS) stars. In their Figure 1, there is a clear trend for larger periods in smaller masses. This trend inevitably implies that stars with lower mass have lower initial rotational speeds.

On the other hand, rotation may reach high initial values for masses where convection is well developed (Costa et al. 2019b). For this reason, in analogy to what we did for the efficiency of convective core overshooting, rotation was not considered for $M_i \leq M_{O1}$ while, for $M_i \geq M_{O2}$, models were computed for the following initial rotation rates: $\omega_i = 0.0, 0.30, 0.60, 0.80, 0.90, 0.95, 0.99$. For stars with an initial mass in the range $M_{O1} \leq M_i < M_{O2}$ we computed models with an initial rotation rate up to a maximum value of

$$\omega_{i,\text{max}}(M) \equiv 0.99 \left(\frac{M - M_{O1}}{M_{O2} - M_{O1}} \right). \quad (2)$$

It is also important to mention that, in this version, the rotation is switched on a few models before the zero-age-main-sequence (ZAMS) phase. At this stage, the code computes the angular velocity Ω that corresponds to the initial rotation rate ω_i and assigns it to each shell of the star, forcing a solid body rotation. From the ZAMS on, the solid body rotation constraint is relaxed, and the stellar rotation evolves accordingly with the conservation and the transport of angular momentum.

2.5. Transport of angular momentum and chemical mixing

The transport of angular momentum is treated based on the pure diffusive approximation (Heger et al. 2000), where the total diffusion coefficient is contributed from three components,

$$D = D_{\text{mix}} + D_{\text{s.i.}} + D_{\text{m.c.}}. \quad (3)$$

where D_{mix} is the diffusion coefficient in the convective zones. The last two terms are related to the shear instability and the meridional circulation. To compute the diffusion coefficient of the shear instability, we use the formula by Talon & Zahn (1997), which reads

$$D_{\text{s.i.}} = \frac{8}{5} \frac{\text{Ri}_c (rd\Omega_r/dr)^2}{N_T^2/(K + D_h) + N_\mu^2/D_h}, \quad (4)$$

where the Brunt-Väisälä frequency is split into N_T^2 and N_μ^2 , $\text{Ri}_c = 1/4$ is the critical Richardson number, K is the thermal diffusivity, and D_h is the coefficient of horizontal turbulence. When angular momentum transport is treated with the diffusive approach, the diffusion coefficient for the meridional circulation remains to be defined. Some authors define it as the product of circulation velocity and its typical length scale (Heger et al. 2000), while others use the same coefficient provided for chemical transport (Chieffi & Limongi 2013a). For the sake of simplicity, we decided to

follow the latter approach. Therefore, we adopt the coefficient by Chaboyer & Zahn (1992), which reads

$$D_{\text{m.c.}} \simeq \frac{|rU|^2}{30D_h}, \quad (5)$$

where U is the radial component of the meridional circulation velocity (see also Maeder 2009; Potter et al. 2012). It should be noted that, as discussed by Chaboyer & Zahn (1992) and Zahn (1992), this coefficient takes into account the net effect of the meridional current and horizontal diffusion for chemical species. A more detailed description of angular momentum transport should include meridional circulation as an advective process. However, due to the difficult numerical implementation of the advective-diffusive treatment, and the fact that the angular momentum redistribution goes in the direction of flattening ω profiles during the main sequence phase (Chieffi & Limongi 2013a), we decided to use the simpler diffusive approach. Future PARSEC versions will include the full advective-diffusive treatment for angular momentum transport. We refer to Costa et al. (2019b) for more details on the numerical implementation of rotation.

Another important difference of this new version, PARSEC V2.0, with respect to PARSEC V1.2S concerns chemical mixing. While in the latter version the gas was chemically homogenized within convective regions, in the present version we adopt a diffusive approach and solve a unique equation for chemical variation due to nuclear reactions, turbulent motions, molecular diffusion, and rotational mixing. The turbulent diffusion coefficient is calculated with the usual approximation $D_T = \frac{1}{3}v_c l_c$ where the velocity of the eddies, v_c , and their mean free path, l_c are obtained from the mixing length theory (Böhm-Vitense 1958).

We note that, while all the above processes can be treated at once, molecular diffusion can be switched off in models where the core overshooting reaches its maximum efficiency (above $M \geq M_{O2}$), because, in such models, the effects of molecular diffusion become negligible with respect to turbulent diffusion and, eventually, rotational mixing. This allows a speed-up of the calculations without loss of generality. We will discuss later the effects brought by adopting either of the mixing schemes described above.

2.6. Mass loss rates

The effects of mass loss in the evolution of low and intermediate mass stars have been extensively studied in many papers (e.g. Reimers 1975; Bloeker 1995; Schröder & Cuntz 2005; Cranmer & Saar 2011; Rosenfield et al. 2014; Kalirai et al. 2008; Catalán et al. 2008; Salaris et al. 2009). In PARSEC models, as well as in previous models of the same group (Girardi et al. 2000b; Bertelli et al. 2008), mass loss was not activated in the calculations of the low-mass tracks but only at the stage of isochrone calculations. This approximation has been tested in many different applications and has always been considered acceptable from our group. It derives from the fact that the RGB evolution of low-mass stars is just marginally affected by this process, which eventually becomes important only very near to the RGB-tip. Therefore, mass loss just causes a decrease in mass between RGB and the stage of “zero-age horizontal branch”. This decrease was easily taken into account when interpolating the helium-burning tracks to prepare isochrones. This method

allows a great flexibility (different mass-loss prescriptions can be tested without recomputing the evolutionary tracks) and speed-up at the level of isochrone calculation. In the more advanced phases of low and intermediate-mass stars, typically from the early up to the end of the thermally-pulsing asymptotic giant branch (TP-AGB) phase, mass-loss is one of the main processes driving the evolution and cannot be neglected. However, the evolution of stars in these phases is computed subsequently with the COLIBRI code (Marigo et al. 2013), where the most updated mass-loss rates are implemented.

With the inclusion of rotation, mass-loss cannot be decoupled from evolution anymore and must be included in all evolutionary phases. This is because rotation may enhance the mass loss, affecting the evolutionary path of the star. This may become dramatic when the star is in proximity to the critical break-up velocity.

In this paper, we apply the Reimers (1975, 1977) law for non-rotating low-mass stars, which is

$$\dot{M}(\omega = 0) = \eta \times 1.343 \times 10^{-5} \frac{L^{1.5}}{m T_{\text{eff}}^2}, \quad (6)$$

where \dot{M} is the mass loss rate in M_{\odot}/yr , L and m are the luminosity and mass in solar units, respectively, and T_{eff} is the effective temperature in K. η is an efficiency coefficient which is generally calibrated against colour-magnitude diagrams of globular clusters, as for instance in Renzini & Fusi Pecci (1988) where the derived η is 0.35, or Aaronson & Mould (1982) who claimed that $\eta = 0.5 - 0.7$ fits well their data of the red globular clusters in the Magellanic Clouds. In this paper, we adopt $\eta = 0.2$, as more recently indicated from the asteroseismic analysis of the two old open clusters NGC 6791 and NGC 6819 by Miglio et al. (2012). As described in Chen et al. (2015), for non rotating intermediate-mass and massive stars we adopt the mass loss rate from de Jager et al. (1988) and Vink et al. (2001), respectively, both corrected by a factor that assumes the same dependence on the surface metallicity, i.e. $\dot{M} \propto (Z/Z_{\odot})^{0.85} M_{\odot}/\text{yr}$.

In the case of rotating stars, the mass-loss rates are enhanced by a factor that depends on the surface tangential velocity, v , as expressed in Costa et al. (2019b,a). By numerically solving the fluid equations of a radiation-stellar wind model, Friend & Abbott (1986) yield a relation where the mass loss rate of a rotating star is modified by a factor with respect to the mass loss of a non-rotating model, which is

$$\dot{M}(\omega) = \dot{M}(\omega = 0) \left(1 - \frac{v}{v_{\text{crit}}}\right)^{-\xi}, \quad (7)$$

where $\xi = 0.43$ is provided in Bjorkman & Cassinelli (1993) by fitting the numerical result of Friend & Abbott (1986). $\dot{M}(\omega = 0)$ is the mass loss rate in case of zero rotation and v_{crit} is the surface critical velocity which is usually defined (Heger et al. 2000) as

$$v_{\text{crit}}^2 = \frac{Gm}{r} (1 - \Gamma_e), \quad (8)$$

G , m , r are the gravitational constant, mass, and radius in solar units, respectively, and Γ_e is the Eddington factor. In this paper, the dependence of Γ_e with the angular velocity is neglected, instead, it should be considered for angular velocities near the critical one (Maeder & Meynet 2000).

3. Evolutionary tracks

Before going into more detail on the analysis of our stellar evolutionary tracks, we summarise some of the main points on the adopted input physics. Firstly, we computed models with six initial metallicities: $Z = 0.004, 0.006, 0.008, 0.01, 0.014, 0.017$ which are relevant for the study of young and intermediate-age star clusters in the Milky Way disk and in the Magellanic Clouds. The initial helium mass fraction follows the enrichment law: $Y = Y_p + \frac{\Delta Y}{\Delta Z} Z$, where $Y_p = 0.2485$ is the primordial He abundance (Komatsu et al. 2011); the helium-to-metal enrichment ratio $\Delta Y/\Delta Z = 1.78$ is based on the solar calibration in Bressan et al. (2012). More specifically, the corresponding initial He mass fraction is $Y = 0.256, 0.259, 0.263, 0.267, 0.273, 0.279$; and the initial hydrogen abundance $X = 0.740, 0.735, 0.729, 0.723, 0.713, 0.704$.

Second, the initial rotation rate is parameterised by ω : for each set of metallicity above, we compute models with rotation rates going from zero to very near the critical point, $\omega_i = 0.00, 0.30, 0.60, 0.80, 0.90, 0.95, 0.99$. The treatment of rotation rate for each single star in terms of mass is described in Sect. 2.4.

Third, the convective overshoot: we apply the overshoot from both the convective core and envelope in the calculations as described in Sects. 2.2 - 2.3.

Lastly, the mass intervals: For convenience, we will describe the evolutionary tracks in three mass ranges: i) very low-mass stars (VLMS) have initial masses $M_i \lesssim M_{\text{vlim}}$, where M_{vlim} is the smallest initial mass of a star that is able to ignite helium within the Hubble timescale. Stars with mass smaller than this limit spend their lifetime mainly on the hydrogen-burning phase; ii) low-mass stars (LMS) have initial masses between M_{vlim} and M_{HeF} , which includes M_{O1} and M_{O2} as mentioned above; and iii) intermediate-mass stars (IMS) with $M_i > M_{\text{HeF}}$. M_{HeF} is defined as the transition mass between stars that develop an electron-degenerate core after the main sequence and hence develop an extended RGB with an He-flash at its tip, and those that do not, hence quietly initiating He-core burning in a non-degenerate core.

Figure 1 shows the dependence of M_{O1} , M_{O2} and M_{HeF} as a function of metallicity, for non-rotating models. We also draw the six metallicities computed in this project. Table 1 lists the values of λ_{ov} and Λ_e adopted for each initial mass.

Finally, the database of all stellar evolutionary tracks that we produced in this work is available at <http://stev.oapd.inaf.it/PARSEC>.

3.1. Very-low-mass stars

The PARSEC models for VLMS ($0.09 M_{\odot} \lesssim M_i \lesssim M_{\text{vlim}}$) were described in Chen et al. (2014) and successfully calibrated against the mass-radius relation of a sample of eclipsing binaries. For this purpose, the authors slightly modified the $T - \tau$ relations provided by PHOENIX (BT-Settl) atmosphere models (see Asplund et al. 2009; Allard et al. 2012). After this calibration, the corresponding isochrones were able to reproduce well the very low ZAMS of old globular clusters NGC 6397 and 47 Tuc, and of the open clusters M67 and Praesepe. These models were also adopted to fit *Gaia* DR2 CMD diagrams (Gaia Collaboration et al. 2018a). Here, we will continue to use these very low-mass

Table 1: The values of core and envelope overshooting parameters, λ_{ov} and Λ_e/H_p respectively, which correspond to each initial mass M_i/M_\odot in six metallicities (Z s). The value of transition masses, M_{vlm} , M_{O1} and M_{O2} , of each metallicities is also noted.

λ_{ov}	Λ_e/H_p	$Z=0.017$ M_i/M_\odot	$Z=0.014$ M_i/M_\odot	$Z=0.01$ M_i/M_\odot	$Z=0.008$ M_i/M_\odot	$Z=0.006$ M_i/M_\odot	$Z=0.004$ M_i/M_\odot	Note
0.000	0.000	< 0.80	< 0.80	< 0.75	< 0.75	< 0.70	< 0.70	M_{vlm}
0.000	0.500	< 1.18	< 1.16	< 1.14	< 1.14	< 1.09	< 1.06	
0.000	0.500	1.18	1.16	1.14	1.14	1.09	1.06	M_{O1}
0.027	0.513	1.20	1.18	1.16	1.16	1.11	1.08	
0.053	0.527	1.22	1.20	1.18	1.18	1.13	1.10	
0.080	0.540	1.24	1.22	1.20	1.20	1.15	1.12	
0.107	0.553	1.26	1.24	1.22	1.22	1.17	1.14	
0.133	0.567	1.28	1.26	1.24	1.24	1.19	1.16	
0.160	0.580	1.30	1.28	1.26	1.26	1.21	1.18	
0.187	0.593	1.32	1.30	1.28	1.28	1.23	1.20	
0.213	0.607	1.34	1.32	1.30	1.30	1.25	1.22	
0.240	0.620	1.36	1.34	1.32	1.32	1.27	1.24	
0.267	0.633	1.38	1.36	1.34	1.34	1.29	1.26	
0.293	0.647	1.40	1.38	1.36	1.36	1.31	1.28	
0.320	0.660	1.42	1.40	1.38	1.38	1.33	1.30	
0.347	0.673	1.44	1.42	1.40	1.40	1.35	1.32	
0.373	0.687	1.46	1.44	1.42	1.42	1.37	1.34	
0.400	0.700	1.48	1.46	1.44	1.44	1.39	1.36	M_{O2}
0.400	0.700	> 1.48	> 1.46	> 1.44	> 1.44	> 1.39	> 1.36	

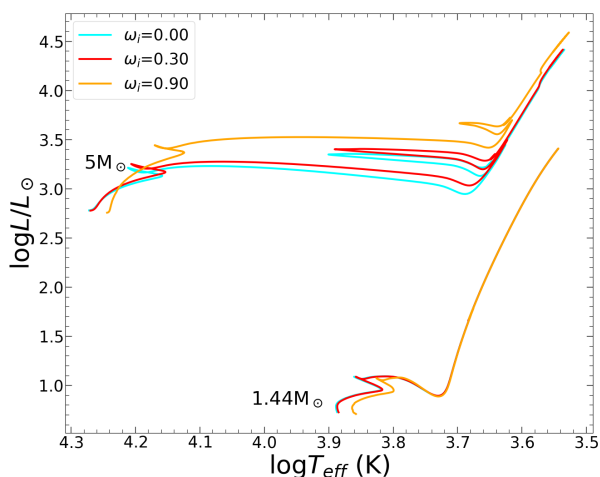


Fig. 2: The Hertzsprung-Russell diagram (HRD) of stars with initial masses of $1.44 M_\odot$ and $5 M_\odot$ with the composition $Z = 0.008$, $Y = 0.263$, for initial rotation rates $\omega_i = 0.00$, 0.30 and 0.90 (cyan, red and orange lines, respectively). We do not plot the evolution on the PMS phase for sake of clarity.

evolutionary tracks, referring to [Chen et al. \(2014\)](#) for all details.

3.2. Low-mass stars

3.2.1. From the pre-main-sequence to the tip of the RGB

We computed models of LMSs with initial masses in the interval from M_{vlm} to M_{HeF} . The mass step is $0.05 M_\odot$ in the mass range from M_{vlm} to $0.8 M_\odot$, $0.02 M_\odot$ for the range

from $0.8 M_\odot$ to M_{O2} , and $0.1 M_\odot$ for masses above M_{O2} . All the LMSs tracks begin from the PMS phase and end at the tip of the red-giant branch (TRGB), where the star ignites its central He under strongly degenerate conditions (the so-called He-flash).

Figure 2 shows the HRD of $1.44 M_\odot$ stars with different initial rotation rates. It should be noted that, for rotating stars, T_{eff} is actually an average value over the isobaric surface; more precisely it is the value that a non-rotating star with the same “volumetric radius” would have to produce the same total luminosity. The volumetric radius is defined as the radius of a sphere with the same volume as that of the rotating star. The local effective temperature characterizing different points at the surface of the star, instead, is a quantity that varies along the co-latitude angle ($\theta = 0^\circ$ aligns with the rotation axis), becoming cooler towards the equator. This can be explained by the proportionality between T_{eff}^4 and effective gravity g_{eff} , based on von Zeipel’s theorem ([von Zeipel 1924b](#); [Espinosa Lara & Rieutord 2007](#)). In turn, the local effective gravity is reduced by the centrifugal force, which is higher for a higher rotation rate. Therefore, as we see in Fig. 2, the higher the rotation rate, the cooler the star is (by means of the average value) during the MS. In the post-MS phases, the conservation of angular momentum forces the surface angular velocity to drop down when the star expands, hence causing the star to evolve along the same path of non-rotating stars.

Another effect of rotation is that the faster the stars rotate, the longer they stay in the MS phase ([Eggenberger et al. 2010](#); [Ekström et al. 2012](#); [Costa et al. 2019a](#)). Fig. 3 shows the ratio of the MS duration between models with different ω_i and their standard non-rotating counterparts, $\omega_i = 0$, as a function of the initial mass M_i and for $Z = 0.01$. We see that this ratio is higher than 1 for all rotating models and becomes higher as ω_i increases. In the low-mass range ($M \lesssim 1.8 M_\odot$) the ratio remains modest, while it increases significantly in the domain of intermediate-mass and

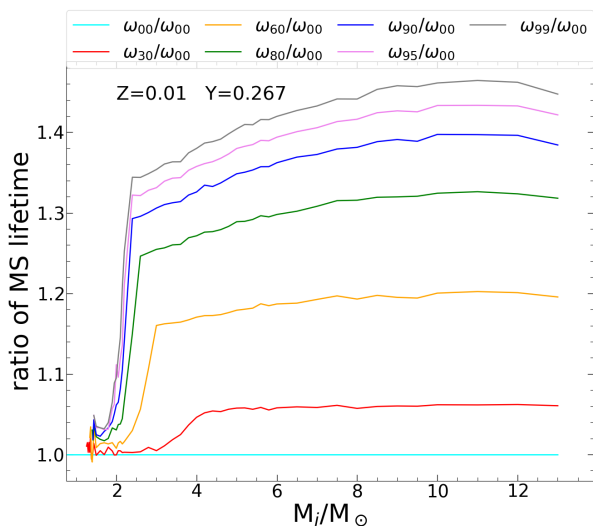


Fig. 3: The ratio between the MS lifetimes between rotating and the non-rotating models of the same mass, as a function of initial mass in the set of $Z = 0.01, Y = 0.267$. This lifetime is measured from the ZAMS until the exhaustion of central-H ($X_c < 10^{-5}$). Different values of ω_i are considered, going from 0 to 0.99 as in the legend.

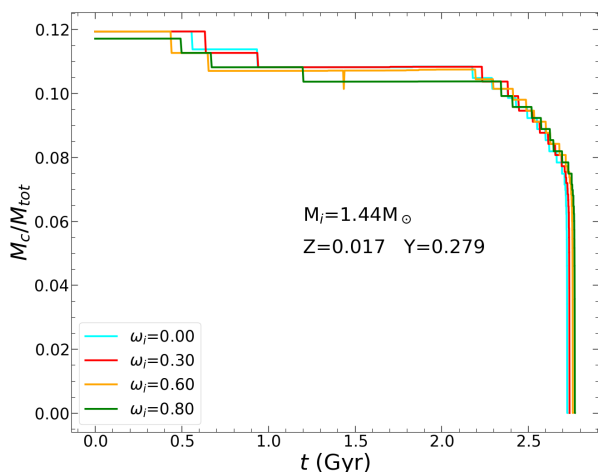


Fig. 4: The time evolution of the mass of the convective core (M_c/M_{tot}) during the H-burning phase for the model of $M_i = 1.44 M_{\odot}$ and $Z = 0.017$.

massive stars. This is understandable because of the lower efficiency of rotational mixing in LMSs with respect to intermediate and massive ones, as will be discussed later in Sect. 3.3.

We also find that in the low-mass range, the size of the convective core does not depend significantly on ω_i . This can be seen in Fig. 4 for the models of $M_i = 1.44 M_{\odot}$ and $Z = 0.017$.

After the formation of the H-exhausted core, the star enters into the sub-giant phase and then ascends the RGB. Expansion of the envelope leads to a decrease in surface rotation velocity. This impact is illustrated in Fig. 5, where the equatorial tangential velocity drastically decreases after

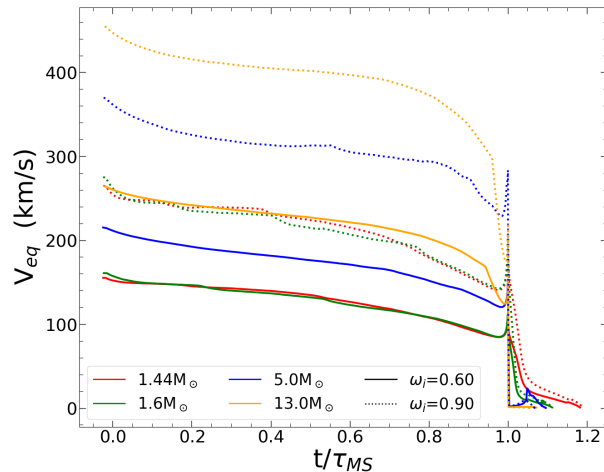


Fig. 5: The evolution of surface tangential velocity at the equator, V_{eq} , versus the time t scaled to the MS duration τ_{MS} . The four selected mass models: $1.44 M_{\odot}$ (red), $1.6 M_{\odot}$ (green), $5 M_{\odot}$ (blue), $13 M_{\odot}$ (orange) are shown, with two initial rotation rates $\omega_i = 0.60$ (solid-line) and $\omega_i = 0.90$ (dotted-line), from the set with $Z = 0.014, Y = 0.273$.

leaving the MS. The drop down on rotation rate results in an evolution as a non-rotating star, as already mentioned and as illustrated in the HRD of Fig. 2. We found that the luminosity at the tip of the RGB phase is almost the same for any applied rotational rates (see also Ekström et al. 2012; Georgy et al. 2013)

For instance, the TRGB luminosity of the $Z=0.004$, $M_i = 1.36 M_{\odot}$ star is $\log L/L_{\odot} = 3.38771$, 3.38934 and 3.38919 for the models with $\omega_i = 0.00$, 0.60 and 0.90 , respectively. We see that the difference is less than 0.0016 dex in any case, and this is due to the slightly heavier He-core mass discussed above. In general, we found that the TRGB luminosity of our models with $M \leq 1.5 M_{\odot}$ is about $\log L/L_{\odot} \sim 3.385 - 3.420$, depending on the initial metallicity. This result is important in the context of the TRGB method of distance determinations, and the recent “tension” in the values of the Hubble constant H_0 (see Freedman et al. 2019, 2020, and references therein for more details).

On the other hand, we also checked the effect of rotation on the mass loss rate. Fig. 6 shows the mass loss rate of the $1.39 M_{\odot}$ model with metallicity $Z = 0.006$, for three initial rotation rates, $\omega_i = 0.00$, 0.30 and 0.95 . We plot $\log \dot{M}$ from the ZAMS to the end of the RGB. As expected from equation (7), during the MS phase the star with higher rotation rates has higher mass loss rates. However, in the RGB phase, because of the decline of the surface rotational velocity, it evolves as a non-rotating star but with a slightly older age. In general, stars lose their mass at a rate of about $(0.6 - 6) \times 10^{-8} M_{\odot}/\text{yr}$ at the TRGB stage. This result is based on the Reimers’ law that we adopted in our models. Interesting alternative models for mass loss have been proposed, Cranmer et al. (2007) and Cranmer & Saar (2011), which will be the subject of other subsequent work. We note that during the stellar contraction phase just after the end of the main sequence, the tangential velocity may reach its critical value, at least for models with the highest initial rotation rates. This is the case for the model with $\omega_i = 0.95$

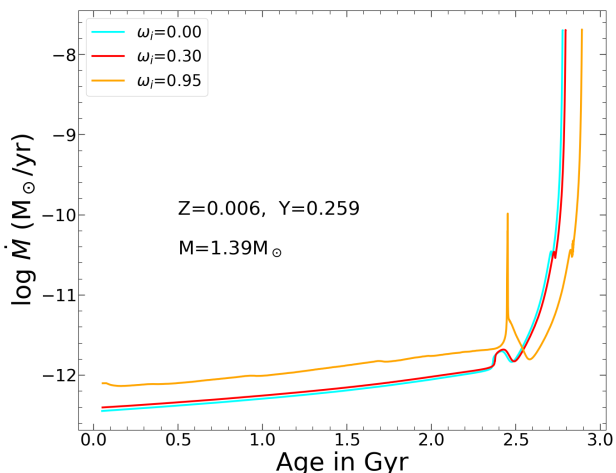


Fig. 6: The mass loss rate as a function of time of star $M_i = 1.39 M_\odot$, $Z = 0.006$ for three rotation rates $\omega_i = 0.00$, 0.30 and 0.95 (cyan, red and orange lines, respectively).

shown in Fig. 6. In this case, the mass loss as provided by equation (7), is enhanced by mechanical effects (Georgy et al. 2013; Costa et al. 2019a) as shown by the relative peak of about two orders of magnitude with respect to the other tracks, before entering the RGB phase.

Concerning the total mass lost on the RGB, we find that it is higher for the smaller initial masses. For non-rotating models of $Z = 0.004$, the stars with initial masses $M_i = 0.9 M_\odot$, $1.16 M_\odot$ and $1.36 M_\odot$ lose about 11%, 6% and 4% of their initial mass, respectively. The total mass lost by the stars at the RGB-tip is illustrated in Fig. 7 for all six sets of metallicity and for two initial rotation rates, $\omega_i = 0.00$ and 0.95 (the solid- and dashed-lines, respectively). From this figure we also see that the key role in the total mass lost by the stars is taken, in decreasing order, by mass, metallicity, and rotation.

Fig. 8 shows the difference in He-core mass at the TRGB between rotating models and their non-rotating counterparts, for three values of $\omega_i = 0.30, 0.60, 0.95$ and for six metallicities. The higher the initial rotation rate, the larger the He-core mass the star has at the tip, at any metallicity. While the surface rotation at this stage is small even for the largest ω_i , in the core it is still significant, as can be seen in Fig. 9. The larger the rotation, the less concentrated is the core, and a larger core mass is needed to reach the conditions for He ignition. At the larger initial masses, there is also a contribution of the more efficient rotational mixing during the main sequence phase. In general, the difference is $\leq 0.006 M_\odot$, depending on ω_i . We note that these differences might affect the location of red clump stars in the HR diagram. This issue will be further investigated in a subsequent work.

3.2.2. From the ZAHB to the TP-AGB

Low-mass stars develop an electron-degenerate core and climb the RGB until they undergo the He-flash. The latter requires large amounts of CPU times to be computed in detail (see Kippenhahn et al. 2012; Mocák et al. 2008, for

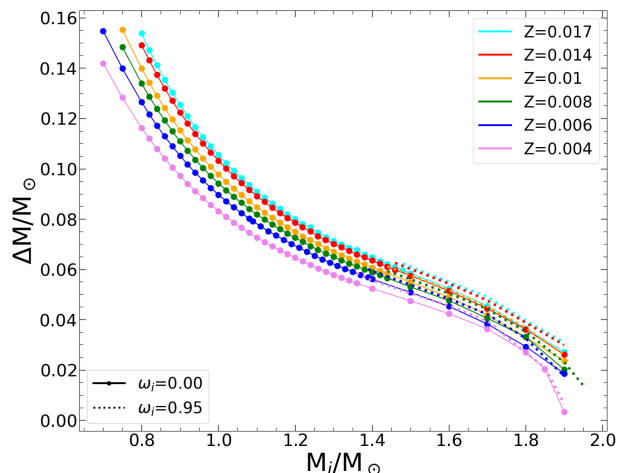


Fig. 7: The total mass lost until the TRGB versus initial mass, for six different metallicity sets. Solid and dashed lines represents models with $\omega_i = 0.00$ and $\omega_i = 0.95$, respectively.

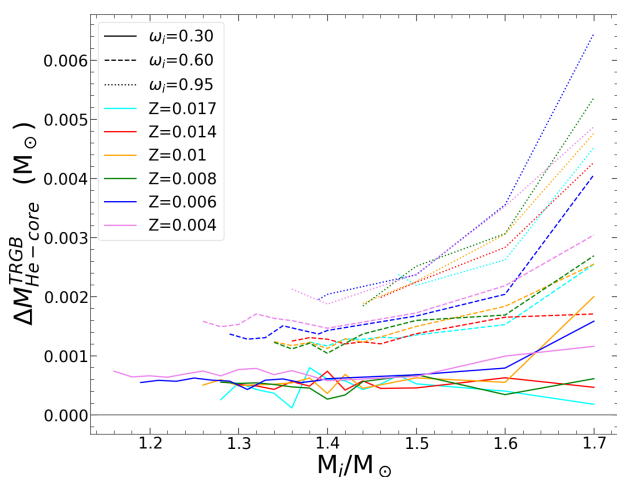


Fig. 8: The difference in He-core mass at the tip of RGB phase between the rotating models and their non-rotating counterparts, $\Delta M_{\text{He-core}}^{\text{TRGB}}$. Three initial rotation rates are considered: $\omega_i = 0.30, 0.60, 0.95$ (solid, dashed and dotted line, respectively). The colours represent different initial metallicities. The grey-solid line marks the reference line for $\omega_i = 0$ models.

more details). Therefore, the computation of the evolutionary track is interrupted during the He-flash, and restarted from a zero-age horizontal branch (ZAHB) model with the same He-core mass and surface chemical composition as the last RGB model. The initial ZAHB model is built following the method described in Bressan et al. (2012), taking into account the fraction of He that has been burned into carbon during the flash so that the degenerate core is lifted into a non-degenerate state. Then, the star is evolved along the Horizontal Branch (HB) and the evolution is terminated again after it experiences a few pulses of the TP-AGB

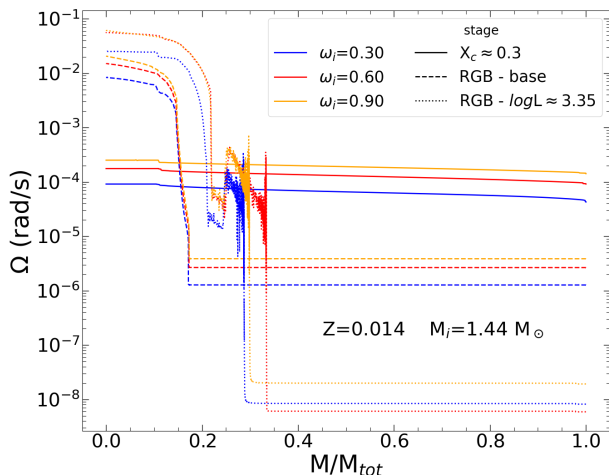


Fig. 9: The internal distribution of angular velocity, Ω . Three selected stages of models with $Z = 0.014$, $M_i = 1.44 M_\odot$ are presented: at which central hydrogen $X_c \approx 0.3$ during the MS (solid lines), at the base of the RGB phase (dashed lines) and near the RGB's tip with $\log L \approx 3.35$ (dotted lines). The colours represent different selected initial rotation models.

phase. The evolutionary tracks in the HR diagram during the post-ZAHB phases of LMS are illustrated in Fig. 10, just for a single set of metallicity. Similar grids are available for all metallicities.

It is important to point out a few details in these calculations:

1. Rotation is turned off for the entire evolution beyond the ZAHB, simply because at those stages the rotational velocities have become small enough to not imply significant evolutionary effects.
2. With respect to the previous version of PARSEC, the new tracks include mass loss starting from the ZAMS. Thus, for any given initial metallicity, we have different relations $M_{\text{TRGB}}(M_i)$ for different ω_i . These relations are merged to obtain a complete unique sequence of $M_{\text{ZAHB}}(M_i)$, with M_{ZAHB}^i spanning the range from the largest M_{TRGB} to the lowest value compatible with the thinnest envelope mass along the ZAHB sequence. We also pay attention to carefully sample the mass interval close to M_{HeF} . We then interpolate on the sequence of non-rotating models to obtain a unique complete $M_{\text{core}}(M_{\text{ZAHB}}^i)$ relation, which is used to construct the ZAHB model sequence.

3.3. Intermediate-mass and massive stars

Intermediate-mass stars (IMSS) are defined as having masses larger than the M_{HeF} limit and smaller than the M_{up} threshold for C ignition in the core. Both limits depend on the initial metallicity and the rotation rate. Massive stars are computed up to $14 M_\odot$, leaving more massive stars to a dedicated paper, which is in preparation. Models with initial masses between M_{HeF} and $2.2 M_\odot$ are computed with a mass step $\Delta M_i = 0.05 M_\odot$; from $2.2 M_\odot$ up to $6 M_\odot$,

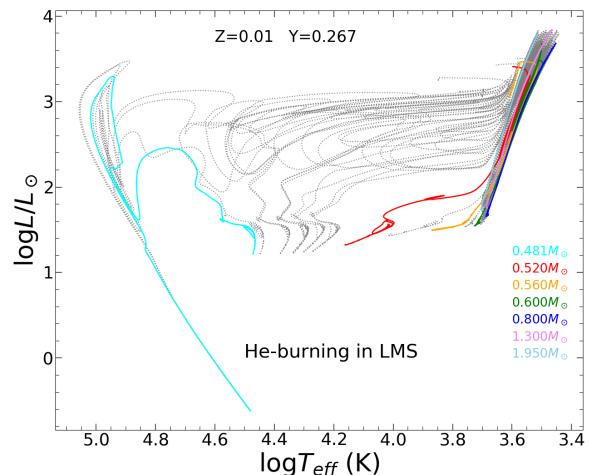


Fig. 10: The He-burning phase of low-mass-stars in the set with $Z = 0.01$, $Y = 0.267$. Tracks with ZAHB masses between 0.481 and $1.95 M_\odot$ were computed in this case. A few of these tracks are marked with a different colour (with their mass in M_\odot indicated in the legend), for reference.

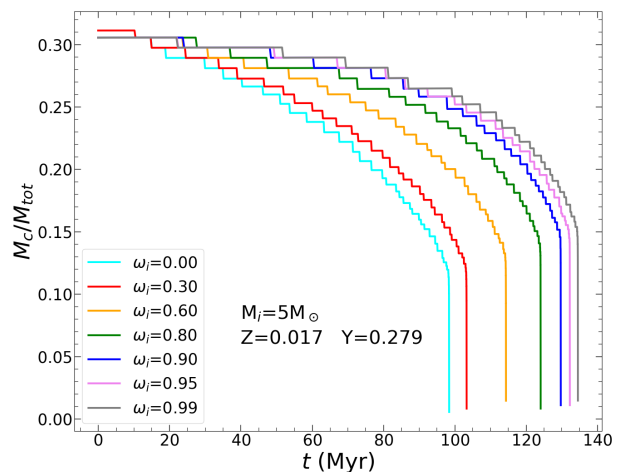


Fig. 11: The evolution of the mass of the convective core (M_c/M_{tot}) during the H-burning phase for the model of $M_i = 5.0 M_\odot$ and $Z = 0.017$.

$\Delta M_i = 0.2 M_\odot$; up to $10 M_\odot$, $\Delta M_i = 0.5 M_\odot$ and $\Delta M_i = 1 M_\odot$ above $M_i = 10 M_\odot$. All these tracks start on the PMS phase and are interrupted either after the first few thermal pulses along the AGB, or after the ignition of carbon in the core. All evolutionary tracks in this mass range have been computed with the maximum overshooting efficiency, i.e. with $\lambda_{\text{ov}} = 0.4$ and $\Lambda_e = 0.7 H_p$ and for all initial rotation rates from $\omega_i = 0.00$ to 0.99 (Sect. 2.4). The mass loss rates of rotating stars follow the description in Sect. 2.6, while the formulation of de Jager et al. (1988) was adopted for non-rotating models.

In Figure 2 we have already compared the evolution of a $5 M_\odot$ model calculated with three different rotation rates, $\omega_i = 0.0, 0.30, 0.90$, with that of a $1.44 M_\odot$ model

with the same ω_i . Rotation impacts the evolution of IMSs in a way different from the LMSs. At the beginning of the evolution, only the geometrical effects of rotation are visible: in both cases, the models that rotate faster are less luminous and cooler. As evolution proceeds, IMSs develop a convective core surrounded by a radiative envelope where the meridional circulation works efficiently. As a result, rotational mixing provides more fresh fuel to the central core, and hence a more massive core is built up (see Fig. 11). This causes the IMSs models that rotate faster to become more luminous and to increase their MS lifetimes significantly (as shown in Fig. 3). Due to the larger core masses, the higher luminosity is maintained during all post-MS evolutionary phases. In contrast, in low-mass models even in the case with the largest rotation rate, the growth of the core is never so high to make it more luminous than the non-rotating one. At lower masses, rotation affects more the effective temperature than the luminosity.

Another consequence of rotational mixing during the MS phase is the transport of nuclear-burned products from the central region to the surface. This effect does not occur in non-rotating stars, until dredge-up events occur when the stars become red giants. In rotating stars, instead, significant mixing can occur at much earlier stages. The most evident effect of this mixing is an enhancement in the surface nitrogen and helium, followed by a depletion of both oxygen and carbon. Fig. 12 shows the evolution of He, C, N, O abundance, luminosity, effective temperature, and ω , in three stars of mass $3 M_{\odot}$, $5 M_{\odot}$, and $9 M_{\odot}$, for several initial rotation rates. The faster the star rotates on the MS, the more N and He appear at the surface, and the more C and O are depleted. The increase/decrease in surface abundances develops gradually during the MS but suddenly jumps up/down during the first dredge-up event that occurs after the end of the MS, when the star becomes a red giant. Afterwards, rotational mixing is no longer efficient, and the surface abundances remain constant until, eventually, the advent of the second dredge-up, which affects the IMS of higher mass, after the core-helium burning phase.

As can be seen in Figs. 2 and 12, the increased rotation rates on the MS also reduce the extension (in T_{eff}) of the blue loop during the central He-burning phase. This is also an effect of the enhanced mixing caused by rotation (see the discussion of Costa et al. 2019a, and references therein).

The transition between LMS and IMS is set at a mass M_{HeF} , above which He ignition takes place quietly in a non-degenerate core. Fig. 13 shows the value of M_{HeF} as a function of initial rotation rates for the six metallicities computed in this paper. The plot has a resolution of $0.05 M_{\odot}$, which is the mass separation between successive tracks computed around this mass range. First, lines of different colours illustrate the well-known dependency of M_{HeF} on the initial metallicity. Second, the dependency of M_{HeF} on initial rotation rate. For instance, the $Z = 0.004$ models have M_{HeF} values of either $1.85 M_{\odot}$ or $1.90 M_{\odot}$, while those with $Z = 0.017$ the values of 2.00 or $2.05 M_{\odot}$. We find that at increasing rotation rates, the value of M_{HeF} also tends to increase with respect to the non-rotating models. However, when the initial rotation rate increases to values close to the critical break-up velocity, M_{HeF} declines again, returning to the value of non-rotating stars. This behaviour of M_{HeF} cannot be discussed in much detail because all changes occur within the mass separation step of $0.05 M_{\odot}$. However, it is

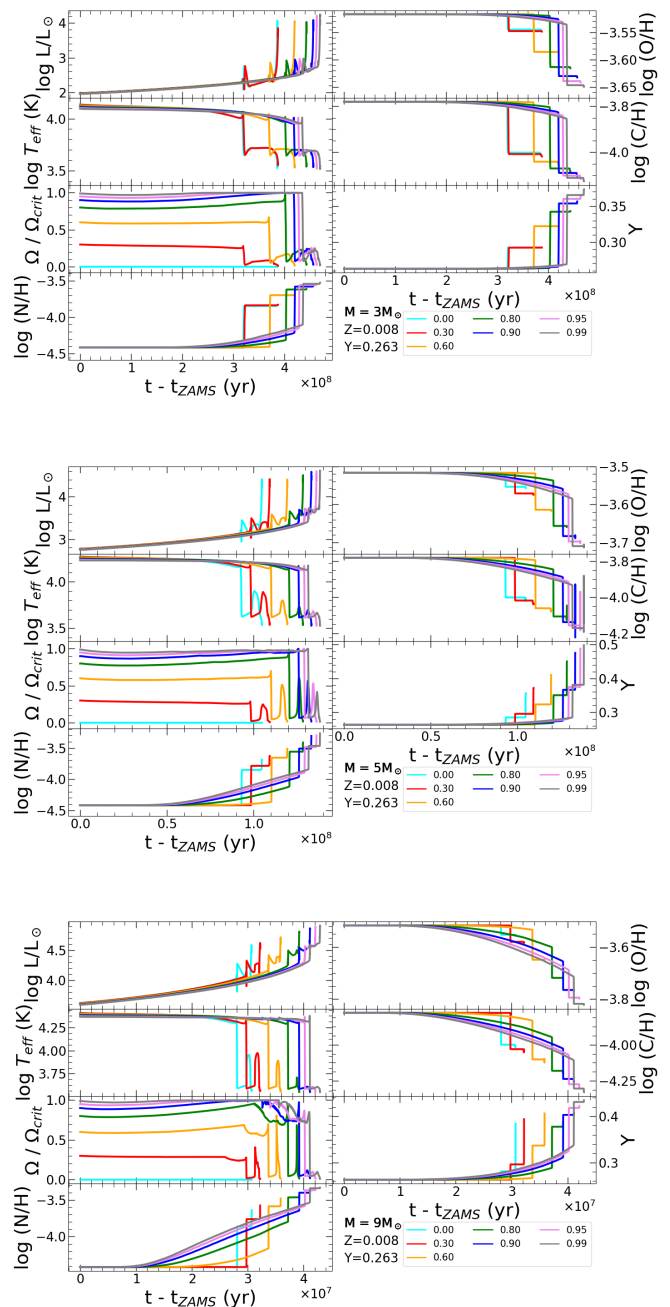


Fig. 12: The evolution of $\log L$, $\log T_{\text{eff}}$, rotation rate ω and surface abundances of N, C, O, and He at the surface for many initial rotation rates from $\omega_i = 0.00$ to 0.99 (from cyan to grey colours respectively), for the cases of 3 , 5 and $9 M_{\odot}$ stars (in the three sets of panels from top to bottom, respectively) with $Z = 0.008$, $Y = 0.263$. The abundances of N, O, and C are by number, and relative to the hydrogen abundance. For He, instead, we present the surface mass fraction Y .

remarkable that rotation appears to have a limited impact on M_{HeF} .

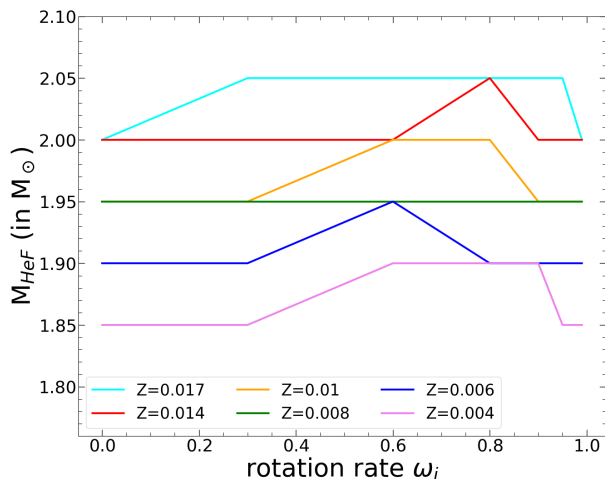


Fig. 13: The maximum mass of which the star burns He in the central region under a strongly degenerative condition, M_{HeF} , versus the initial rotation rates. The colour refers to six computed metallicities in this paper as written in label.

3.4. Comparison with parsec V1.2S and other databases

In Figure 14 we show a comparison between the selected tracks calculated with the new version of the code, PARSEC V2.0, hereafter PS2, and with the older version, V1.2S, hereafter PS1. In both versions, we use the same initial chemical composition. In the leftmost panel, we show the case of a low-mass star with $M_i = 0.8 M_\odot$. Since this star does not possess a convective core during the H-burning phase, the HR diagram is the same for the two versions.

Instead, we recall that during the RGB evolution in the older version, PS1, overshooting at the bottom of the convective envelope has not been considered in the mass range ($\leq M_{01}$), producing RGB bumps (RGBBs) that were too luminous with respect to the observed ones (Fu et al. 2018). To cope with this evident discrepancy, in the new version PS2, we include EOV in low-mass stars as described in Sects. 2.2 - 2.3. The effect of adding an extra mixing at the bottom of the convective envelope is highlighted in the inset of the left panel in Fig. 14, where the RGBBs of stars with masses $0.8 M_\odot \leq M_i \leq 1.4 M_\odot$, are shown.

However, in the mass range where stars develop a convective core in the main sequence (as in the case of $M_i = 1.4 M_\odot$), COV and EOV are fully considered in both versions of the PARSEC code. In PS2, we adopt a smaller value of the maximum core overshooting parameter $\lambda_{\text{ov,max}} = 0.4$, instead of the $\lambda_{\text{ov,max}} = 0.5$ in PS1. Furthermore, in PS2 we adopt a diffusive treatment for convective mixing, where the diffusion equations are coupled with the nuclear reaction rates for all elements in the turbulent regions. In the PS1 version, the convective zones are “instantaneously” homogenized at every time step. These differences already affect the MS phase of stars with convective cores (with $M_i > M_{01}$), as shown in the middle panel in Fig. 14. The PS2 track with $1.4 M_\odot$ presents a hotter and slightly fainter MS phase, and a fainter sub-giant phase.

On the other hand, the RGB phase has the same slope in both versions of PARSEC tracks. The new tracks show a brighter and cooler RGB-tip. These differences in the

TRGB are caused by the more massive He-core and the more extended envelope at the tip. This is mainly due to the different overshoot parameters used in PS2 and the fact that in this new calculation mass loss was implemented along the evolution while, in PS1, models were evolved at constant mass, and mass loss was applied at the stage of isochrone calculation only.

In Fig. 15, we compare the luminosity at the RGB-tip of the PS2 models with that of PS1, BaSTI (Bag of Stellar Tracks and Isochrones, Hidalgo et al. 2018) and MIST (MESA Isochrones and Stellar Tracks, Choi et al. 2016) evolutionary tracks. The latter two databases also include convective overshooting and diffusion in their models. We can see that PS2 predicts a quite constant TRGB luminosity and, generally, above the luminosity of other models shown in the plot. The difference between the new and old versions of PARSEC is about $\sim 0.01 - 0.02$ dex. BaSTI gives an increased trend of TRGB luminosity with initial masses, which is in contrast with the trend from MIST. PS2’s TRGBs are ~ 0.04 dex brighter than MIST.

The right-hand panel of Figure 14 shows the comparison between non-rotating models of intermediate-mass stars of the two PARSEC code versions. In this case, the impact of the core overshooting parameter is clear. The difference between PS1 and PS2’s tracks starts from the MS and continues up to the He-burning phase. In particular, the new tracks are less luminous than the previous ones, due to their smaller $\lambda_{\text{ov,max}}$ value.

Recently, Amard et al. (2019) published grids of STAREVOL models in which rotation is included for masses from $0.2 M_\odot$ to $1.5 M_\odot$. STAREVOL tracks are provided for three values of initial rotation rates, $\omega_i = 0.20, 0.40$ and 0.60 , while in this work we provide $\omega_i = 0.30, 0.60, 0.80, 0.90, 0.95, 0.99$. To facilitate the comparison, we perform a few PARSEC V2.0 calculations with exactly the same initial composition ($Z = 0.0134$ and $Y = 0.269$) and the same initial rotation rate as STAREVOL. Fig. 16 compares the models of $1.3 M_\odot$ and $1.5 M_\odot$ produced by both PARSEC v2.0 (red line) and STAREVOL (green line). The differences between our and STAREVOL models are significant. First, the STAREVOL tracks evolve until the end of the MS phase, while our tracks extend up to the He-flash. Second, for the same initial mass, rotation rate, and composition, our MS stars are hotter and brighter. This might be explained by the many differences in the input physical parameters between the two codes. For example, Amard et al. (2019) do not include overshooting in their calculations, while we consider it for both the convective core and the envelope. Third, there are differences in the implementation of rotation in each codes, namely, STAREVOL implements rotation from the PMS while we assign the rotation (and let it evolve) just before the ZAMS. It is also worth mentioning that there are other differences between the two codes, e.g. they adopt the mixing-length parameter $\alpha_{\text{MLT}} = 1.973$ and the nuclear reaction rates from the NACRE II database (Xu et al. 2013).

However, despite the differences listed above, the two codes give similar ages at the terminal-age-MS (TAMS). For instance, for the $1.3 M_\odot$ star with $\omega_i = 0.2$ PS2 gives 3.74 Gyr while STAREVOL gives 3.94 Gyr.

Another similarity is in the mass loss rates: at the TAMS, the $1.5 M_\odot$ star with $\omega_i = 0.6$ loses its mass with a rate of $\log \dot{M} = -11.70$ (M_\odot/yr) in PS2 while STAREVOL gives $\log \dot{M} = -11.62$ (M_\odot/yr), even though the codes use different schemes for the mass loss rate. In particular, we use

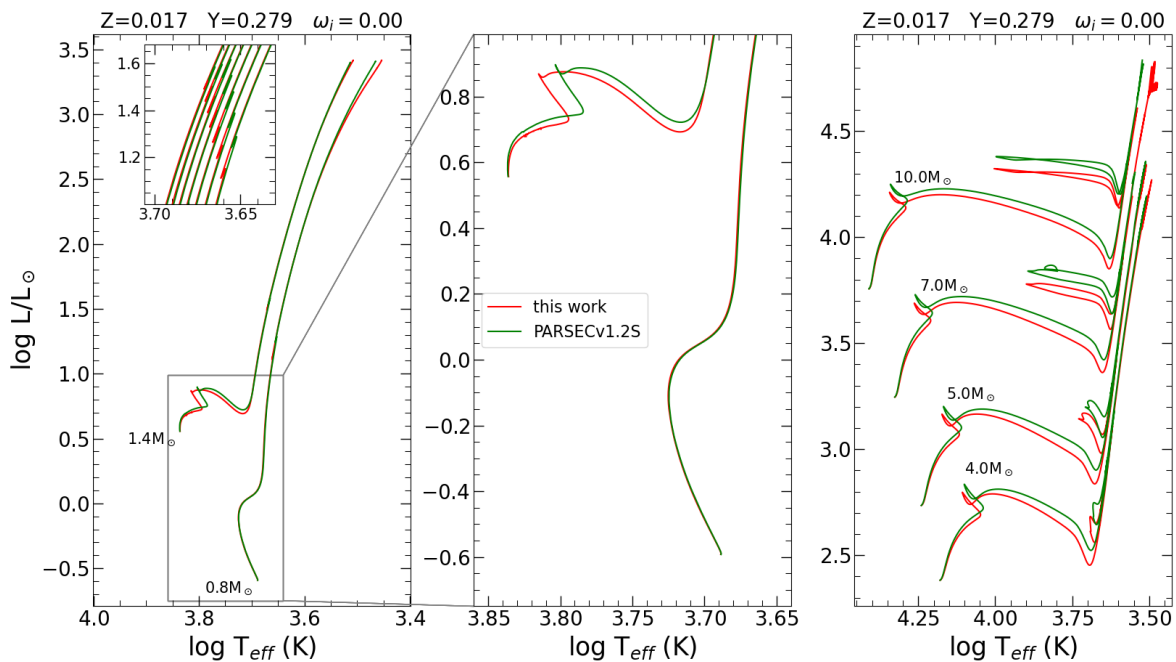


Fig. 14: HRD comparing tracks between PARSEC v2.0 (this work, red lines) and the previous version (PARSEC v1.2S, green lines) for non-rotating stars of $Z = 0.017$ and $Y = 0.279$. The left-hand panel shows the HRD of two low-mass stars with 0.8 and $1.4 M_{\odot}$. Their PMS phase is not shown, because it is essentially the same in the two versions. The inset details the region around the RGB bump for tracks in the mass range from 0.8 to $1.4 M_{\odot}$ with a step of $0.1 M_{\odot}$. The middle panel zooms in the MS regions of the 0.8 and $1.4 M_{\odot}$ tracks. The right panel instead compares intermediate-mass models for four different masses as indicated.

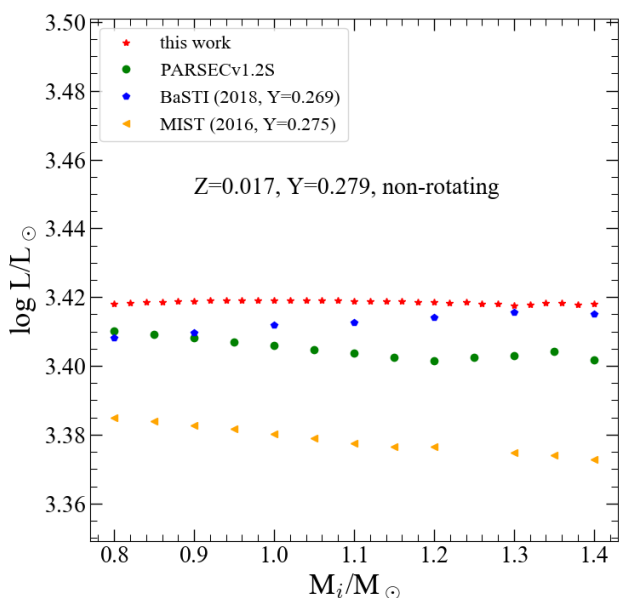


Fig. 15: The luminosity at the tip of RGB as a function of initial mass for the tracks produced in this work (with $\omega_i = 0$; red stars), in parsec v1.2S (green circles), and BaSTI (blue pentagons). The BaSTI tracks for solar-scaled composition are taken from [Hidalgo et al. \(2018\)](#) with $Z = 0.01721$, $Y = 0.2695$.

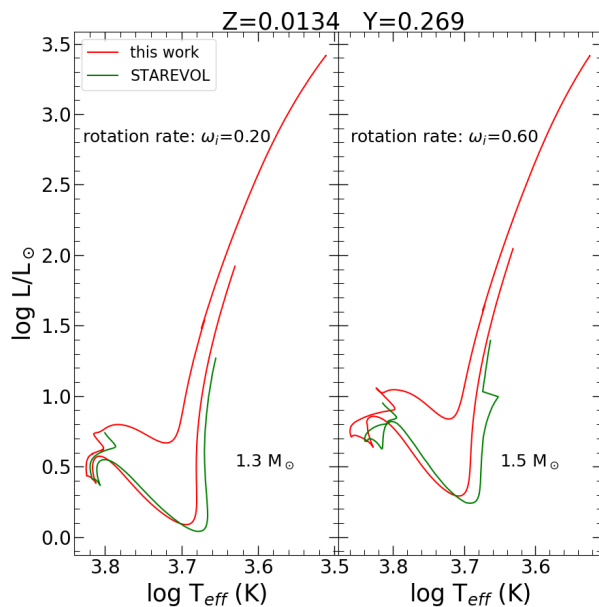


Fig. 16: The comparison on HRD of rotating tracks between this work (red lines) and STAREVOL (green lines) with the same $Z = 0.0134$ and $Y = 0.269$. Left-hand panel: slow-rotating tracks with $\omega_i = 0.20$ of $1.3 M_{\odot}$ star. Right-hand panel: the same as the left panel but with $\omega_i = 0.60$ and $M_i = 1.5 M_{\odot}$.

the enhanced formula from the Reimers law with $\eta = 0.2$ for rotating stars while STAREVOL uses the recipe of [Cranmer & Saar \(2011\)](#). However, we should note that at these early stages, the mass loss does not play a crucial role yet.

4. Isochrones

For all sets of evolutionary tracks described in the previous sections, we have constructed the corresponding isochrones. The initial phase begins from the PMS, and the final stage is either the beginning of the TP-AGB phase for low- and intermediate-mass models or the C-exhaustion for higher masses. As explained in Sect. 2.4, at a given initial metallicity and rotation rate, a certain number of low-mass models were not computed, due to our choice of decreasing ω_{\max} at decreasing M_i , in the transition towards low-mass stars (Eq. 2). While computing the isochrones, the missing tracks of a given ω_i are replaced by the track with the nearest initial mass in the set of tracks with the same metallicity and with ω_i immediately smaller. This ensures that the isochrones gradually shift from the required ω_i to the non-rotating case in the mass interval between M_{02} and M_{01} .

After selecting all the stellar tracks in each set, based on the initial metallicity and rotation rate, the computation of isochrones proceeds in the following steps: first, the computed stellar evolutionary tracks in each set are homogeneously divided into phases separated by a few characteristic “equivalent evolutionary points”. Then, for a given age, the isochrone is constructed by interpolating all stellar properties between points of different initial mass but equivalent evolutionary stage. More details of the interpolation scheme can be found in [Bertelli et al. \(1990b\)](#) (see also [Bertelli et al. 2008](#)). In this paper, the isochrones are produced by a recent version of the TRILEGAL code ([Girardi et al. 2005](#); [Marigo et al. 2017](#)), which interpolates all the additional quantities needed to characterize rotating stars. Several isochrones have been produced with metallicity in the range from 0.004 to 0.017 in steps of 0.001 and ages in the range from 10 Myr to ~ 13 Gyr at intervals of 0.05 in the scale log and for the seven sets of initial rotation rates from zero to $\omega_i = 0.99$. As an example, the left-hand panel of Fig. 17 shows the theoretical isochrones of non-rotating stars for several ages and metallicities.

The theoretical isochrones provide the intrinsic properties of the stars, such as, for instance, the luminosity, mean effective temperature, angular velocity, radius at pole and equator, etc. Then they are complemented with photometric magnitudes in several filters for comparison with observed colour-magnitude diagrams. For non-rotating stars, this is usually done by using tables of bolometric corrections (BCs) as a function of effective temperature, surface gravity and metallicity (see [Girardi et al. 2002](#)); eventually these tables also consider the interstellar extinction in a star-to-star basis, as in [Girardi et al. \(2008\)](#). The right-hand panel of Fig. 17 shows non-rotating isochrones in the *Gaia* passbands, corresponding to those shown in the left-hand panel, where *Gaia* EDR3 photometry is adopted (see [Riello et al. 2021](#)).

BC tables for rotating stars have at least two more parameters than those for non-rotating stars: the rotation rate ω and the inclination angle, i , of the line of sight with respect to the stellar rotation axes. Such BC tables are described in [Girardi et al. \(2019\)](#). They are already imple-

mented in the YBC database³ of BCs by [Chen et al. \(2019\)](#), and in the TRILEGAL code we use to produce the present isochrones. The left-hand panel of Fig. 18 shows some selected rotating isochrones. The two panels on the middle and right-hand side of Fig. 18 illustrate the result of applying the BCs to isochrones with rotation ω_i , and how the photometry changes when observing rotating stars from $i = 0^\circ$ (pole-on) and $i = 90^\circ$ (equator-on). The changes in the photometry are the most remarkable for the stars close to the upper main sequence, since those are the stars which still retain a large fraction of their initial rotational velocity.

For cool red giants, the BC tables for rotating stars do not cover the complete range of low effective temperatures that might be necessary to build the isochrones containing fast-rotating stars. For instance, for $\omega = 0.9$ and $\log g = 2$ the BC tables defined in [Girardi et al. \(2019\)](#) are limited to effective temperatures above ~ 4000 K. Fortunately, inspection of our final isochrones reveals that this limitation is not a practical problem: it turns out that all giants with T_{eff} smaller than ~ 5000 K are slow rotators, with $\omega \lesssim 0.2$. Since these slow rotators have nearly spherical configurations, we decide to apply the BC tables for non-rotating stars from [Chen et al. \(2019\)](#) (YBC) to all stars with $T_{\text{eff}} < 5250$ K, for all values of ω_i . This choice ensures a smooth behaviour of the colours, as can be appreciated in the middle and right panels of Fig. 18.

The database of isochrones in several photometry systems is available in <http://stev.oapd.inaf.it/cmd>.

5. Discussion and Conclusions

We have presented a new library of evolutionary tracks with rotation for low- and intermediate-mass stars produced with PARSEC V2.0. Masses from $0.09 M_\odot$ to $14 M_\odot$ and metallicity Z between $Z=0.004$ and $Z=0.017$ are considered, for seven values of the initial rotation rate in the range $\omega_i = 0.00 - 0.99$. The major differences between the last version of PARSEC, V2.0 and the previous one are, i) the inclusion of rotation; ii) The inclusion of mass loss along the evolution of all the stars because, for rotating models, it constitutes an important sink of angular momentum ([Friend & Abbott 1986](#)); iii) the treatment of turbulent mixing as a diffusive process together with rotational mixing, nuclear processing, and, molecular diffusion (for low-mass stars). In particular, concerning the last point, we recall that, to estimate the efficiency of overshooting from the convective core, we were guided by the work of [Costa et al. \(2019b\)](#), where the maximum core overshooting parameter has been calibrated in a well-studied sample of eclipsing binary systems ([Claret & Torres 2018](#)), obtaining $\lambda_{\text{ov}} = 0.4$.

We also calculated the isochrones up to the beginning of the TP-AGB phase or up to the end of the central C-burning phase. Using the TRILEGAL code, they can be interpolated in metallicity, between $Z = 0.004$ and 0.017 , and in the age range $7.0 \leq \log(t/\text{yr}) \leq 10.1$.

To illustrate some important consequences of the above differences, we show in Fig. 19 and Fig. 20 two preliminary fits to the observed CMD of the open clusters M67 and NGC 6633, respectively. M67 (NGC 2682) is a well known test-bench for study the internal physics of stellar models of low-mass stars with typical turn-off masses around 1.2

³ <https://sec.center/YBC>

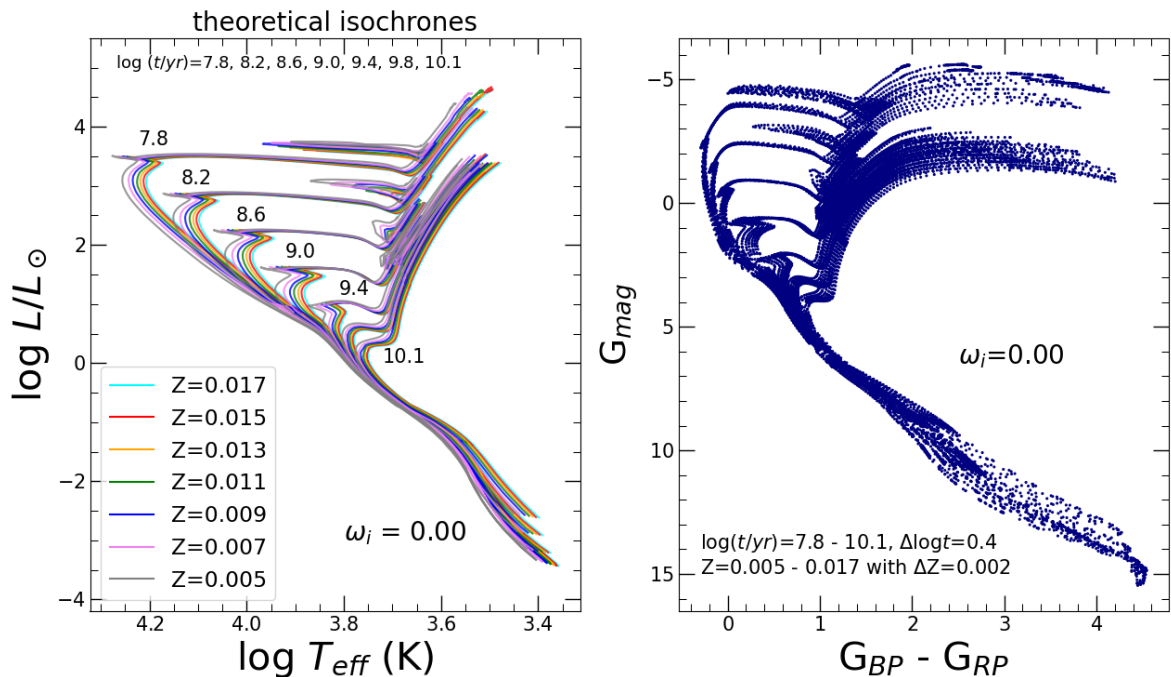


Fig. 17: Theoretical isochrones calculated with the TRILEGAL code. Left-hand panel: isochrones of non-rotating models for the ages $\log(t/\text{yr}) = 7.8, 8.2, 8.6, 9.0, 9.4, 9.8, 10.1$, and seven different metallicities from 0.005 to 0.017, are shown in different colours from gray to cyan, as in the legend. Right-hand panel: the corresponding colour-magnitude diagram in *Gaia*-passbands of the theoretical isochrones shown in the left panel.

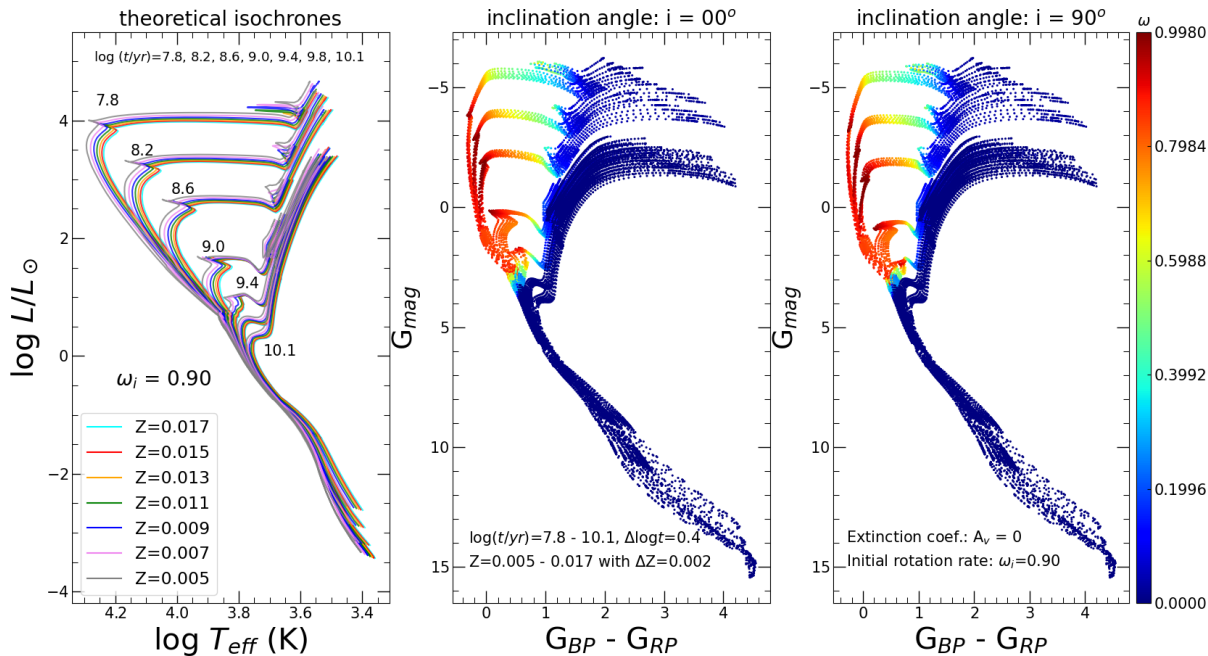


Fig. 18: Left-hand panel: theoretical isochrones with the same parameter of $\log t$ s and Z s as in Fig. 17 but for $\omega_i = 0.90$ set. The middle and right-hand panels: the corresponding colour-magnitude diagram in the *Gaia*-passbands for two values of the inclination angle: $i = 0^{\circ}$ (pole-on) and $i = 90^{\circ}$ (equator-on). Changes in the rotation rate along the isochrones are indicated by the colour bar.

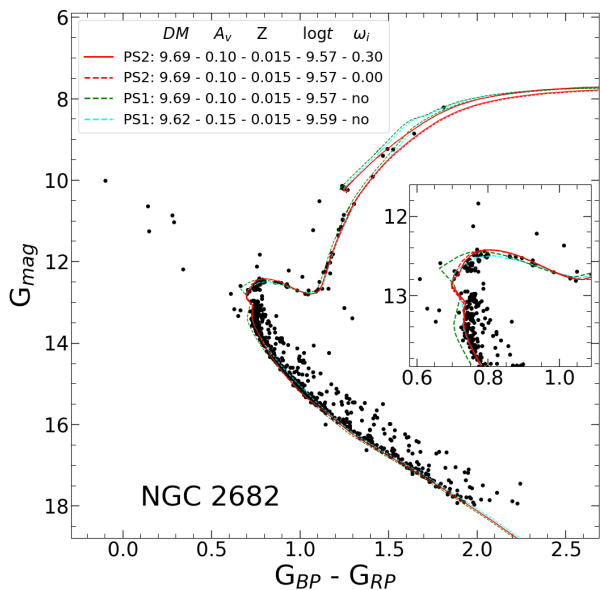


Fig. 19: The CMD of open cluster M67 (NGC 2682) from GDR2 data, overplotted by the isochrones that are produced in this work (solid- and dashed-red lines, labeled by PS2) and those from previous version PARSEC V1.2S (dashed-green and cyan lines, labeled by PS1). The parameters of the isochrones, $DM=(m-M)_0$, A_V , Z, $\log t/\text{yr}$ and ω_i , are displayed in the legend. The inset figure zooms into the turn-off region of this cluster.

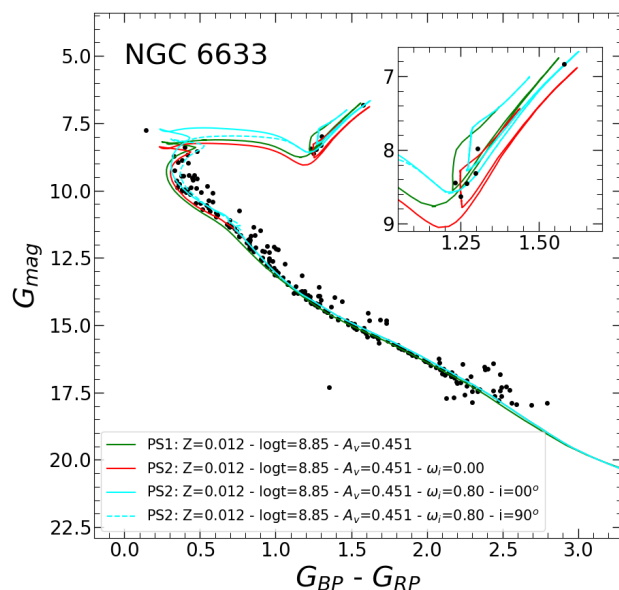


Fig. 20: The CMD of the open cluster NGC 6633 from GDR2. The displayed isochrones are for metallicity $Z = 0.012$, $\log(t/\text{yr}) = 8.85$, $(m-M)_0 = 7.841$ and $A_V = 0.451$ mag. The red-line represents the non-rotating case while the two cyan-lines are for rotating isochrones with the same $\omega_i = 0.80$, and inclination angles $i = 0^\circ$ (solid-line) and $i = 90^\circ$ (dashed-line), respectively. The green line is the isochrone obtained with PARSEC V1.2S assuming the same parameters of the previous non-rotating case.

M_\odot . In particular, its CMD was used to calibrate the efficiency of convective overshooting, due to the well-developed convective core in stars around its turn-off region. Furthermore, the cluster, together with other known open clusters, was also used to obtain the age-metallicity relation for the Milky Way disc stars (e.g. Viscasillas Vázquez et al. 2022). Its age has been repeatedly estimated over the years: Sarajedini et al. (2009) reported an age between 3.5 and 4.0 Gyr; from the asteroseismic properties of the giant and red clump stars, Stello et al. (2016) derived an age of the cluster of 3.46 ± 0.13 Gyr; more recently, using the data from the *Gaia* Second Data Release (hereafter GDR2), Bossini et al. (2019) derived a distance modulus $(m-M)_0 = 9.726$ mag, an interstellar extinction coefficient $A_V = 0.115$ mag and an age of 3.639 ± 0.017 Gyr (see Arenou et al. 2018; Gaia Collaboration et al. 2018a,b; Lindegren et al. 2018, for more details about GDR2).

The M67 CMD, shown in Fig. 19, has been obtained from the data provided by Cantat-Gaudin et al. (2018) who determined photometry, memberships, mean distances, and proper motions of stars in 1229 open clusters. It should be noted that the stars are limited to apparent $G \leq 18$ mag to keep the photometric precision in *Gaia*'s passbands at the level of a few millimag (see Godoy-Rivera et al. 2021; Bossini et al. 2019; Evans et al. 2018, for more details). Also plotted in Fig. 19 are a number of our isochrones selected with the following criteria. Lines labeled PS2 indicate our best fit PARSEC V2.0 isochrones. The fit has been obtained by adopting the distance modulus obtained by Bossini et al. (2019), $(m-M)_0 = 9.726$ mag, but correcting it for a zero-

point offset of $-30 \mu\text{arcsec}$ (Lindegren et al. 2018). The final corrected distance modulus is $(m-M)_0 = 9.69$ mag. For an initial composition of $Z = 0.015$ ($[\text{Fe}/\text{H}] \sim 0$), $Y = 0.275$ (our corresponding He value), the best fit has been obtained adopting an extinction $A_V = 0.1$ mag and an age of $\log(t/\text{yr}) = 9.57$. Plotted in the figure are both a non-rotating isochrone (dashed red line) and one for a slow rotation (solid red line). For both isochrones we use the same best fit parameters because the adopted low rotation affects only marginally the region above the cluster turn-off.

In the same figure, we show also the results we obtain using PARSEC V1.2S, labeled “PS1”. For the model represented by the green dashed line we adopt the same fit parameters of the PS2 solutions. The inset in the figure zooms the turn-off region to highlight the differences between the isochrones. We see that this PARSEC V1.2S isochrone has a more pronounced hook, at the same fitting parameters. This is an evident feature of models computed with a larger core overshooting parameter. Instead, the cyan dashed isochrone was drawn to reproduce the fit obtained with PS1 models, keeping fixed only the metallicity and letting the other parameters to vary within reasonable uncertainties. For this second PS1 model, that runs almost on top of the PS2 isochrones, we adopt a slightly shorter distance modulus, $(m-M)_0 = 9.62$, a larger extinction, $A_V = 0.15$ mag, and a 5% older age $\log(t/\text{yr}) = 9.59$. We note that all the four isochrones run almost superimposed onto one another in the subgiant branch which, being an almost horizontal feature in the CMD, is a robust indicator of the apparent distance.

The new fitting parameters result from the need to diminish the hook extension that, with PARSEC V1.2S, can be done only by using a slightly older age for a fixed metallicity. The variation of the distance modulus and the attenuation almost compensate each other but the latter is also needed to improve the fitting of the colours of the turn-off region. The differences of the parameters between the latter fit and the PS2 ones should be representative of the differences obtained by using the new version of PARSEC instead of the previous V1.2S version, in this age domain.

Recently, it has been shown that M67 harbours an interesting spectroscopic binary system located near the turn-off region, WOCS 11028, that challenges theoretical models (see Sandquist et al. 2021, for a thorough discussion). Briefly, the mass of the primary component is estimated to be $M_{WOCSa} = 1.222 \pm 0.006 M_{\odot}$ while, current predictions using different stellar evolution codes (including PARSEC V1.2S), give values that are lower by $\delta m = 0.05 M_{\odot}$, i.e. about 8σ lower. We confirm that we get the same result also with the new version of PARSEC and leave this problem to a more exhaustive investigation using new PARSEC models at varying initial metallicity and He content (see also Sandquist et al. 2021).

Another object we present in this paper as a preliminary check of the new models is the young open cluster NGC 6633, also present in the GDR2's catalogue. High-resolution spectroscopy for NGC6633 comes from the analysis by Casamiquela et al. (2021) who studied the age metallicity relation of the Milky Way using 47 open clusters observed with *Gaia*. Bossini et al. (2019) derived for NGC 6633 $(m - M)_0 = 7.866^{+0.024}_{-0.025}$ mag, $\log(t/\text{yr}) = 8.888^{+0.006}_{-0.032}$ and $A_V = 0.451^{+0.025}_{-0.02}$ mag. With the same procedure used for M67, we fit the CMD of NGC 6633 with the new isochrones adopting $Z = 0.012$, $Y = 0.270$, $A_V = 0.451$ mag and distance modulus $(m - M)_0 = 7.841$ mag including $-30\mu\text{arcsec}$ offset in *Gaia* parallaxes, and the age of $\log(t/\text{yr}) = 8.85$ (Fig. 20). Both non-rotating and rotating isochrones are displayed with values indicated in the corresponding labels. The lower MS is very well fitted while the extended MS turn-off region is fully reproduced by rotating isochrones taking also into account the effects of inclination angles that, in this cluster, are clearly seen. Furthermore, the different rotational velocities in this cluster can also explain the particular feature visible near the red clump. Indeed, if only rotating models were used, as needed by the fit of the TO region, it would have been difficult to explain the position of the three stars that fall clearly below the corresponding He clump, given the corresponding much shorter evolutionary lifetimes. They are instead fully compatible with the He clump of non-rotating models of similar age. Thus even in NGC 6633 there are hints for the presence of at least one population of non-rotating stars and another of fast rotators, as in the case of the young LMC cluster NGC 1866 (Costa et al. 2019a).

Acknowledgements. GC acknowledges financial support from the European Research Council for the ERC Consolidator grant DEMOBLACK, under contract no. 770017. LG and PM acknowledge financial support from Padova University, Department of Physics and Astronomy Research Project 2021 (PRD 2021). AB acknowledges funding from PRIN MIUR 2017 prot. 20173ML3WW 001 and 002, 'Opening the ALMA window on the cosmic evolution of gas, stars and supermassive black holes'. CY and XF acknowledge the science research grants from the China Manned Space Project with NO. CMS-CSST-2021-A08. YC acknowledges the financial support from the National Natural Science Foundation of China (12003001) and the Na-

tional Key R&D Program of China (2021YFC2203100). XF thanks the support of China Postdoctoral Science Foundation No. 2020M670023, the National Key R&D Program of China No. 2019YFA0405500 and the National Natural Science Foundation of China (NSFC) under grant No.11973001, 12090040, and 12090044. PG acknowledges support provided by NASA through grant HST-AR-15023 from the Space Telescope Science Institute, which is operated by the Association of Universities for Research in Astronomy, Inc., under NASA contract NAS5-26555.

References

- Aaronson, M. & Mould, J. 1982, ApJS, 48, 161
Allard, F., Homeier, D., & Freytag, B. 2012, Philosophical Transactions of the Royal Society of London Series A, 370, 2765
Alongi, M., Bertelli, G., Bressan, A., & Chiosi, C. 1991, A&A, 244, 95
Amard, L., Palacios, A., Charbonnel, C., et al. 2019, A&A, 631, A77
Aparicio, A., Bertelli, G., Chiosi, C., & Garcia-Pelayo, J. M. 1990, A&A, 240, 262
Arenou, F., Luri, X., Babusiaux, C., et al. 2018, A&A, 616, A17
Asplund, M., Grevesse, N., & Jacques Sauval, A. 2006, Nucl. Phys. A, 777, 1
Asplund, M., Grevesse, N., Sauval, A. J., & Scott, P. 2009, ARA&A, 47, 481
Bertelli, G., Betto, R., Bressan, A., et al. 1990a, A&AS, 85, 845
Bertelli, G., Betto, R., Bressan, A., et al. 1990b, A&AS, 85, 845
Bertelli, G., Bressan, A., Chiosi, C., & Angerer, K. 1986, A&AS, 66, 191
Bertelli, G., Bressan, A. G., & Chiosi, C. 1984, A&A, 130, 279
Bertelli, G., Girardi, L., Marigo, P., & Nasi, E. 2008, A&A, 484, 815
Bjorkman, J. E. & Cassinelli, J. P. 1993, ApJ, 409, 429
Bloeker, T. 1995, A&A, 297, 727
Böhm, K. H. 1958, ZAp, 46, 245
Böhm-Vitense, E. 1958, ZAp, 46, 108
Bossini, D., Miglio, A., Salaris, M., et al. 2015, MNRAS, 453, 2290
Bossini, D., Vallenari, A., Bragaglia, A., et al. 2019, A&A, 623, A108
Bressan, A., Bertelli, G., & Chiosi, C. 1986, Mem. Soc. Astron. Italiana, 57, 411
Bressan, A., Fagotto, F., Bertelli, G., & Chiosi, C. 1993, A&AS, 100, 647
Bressan, A., Marigo, P., Girardi, L., et al. 2012, MNRAS, 427, 127
Bressan, A. G., Chiosi, C., & Bertelli, G. 1981, A&A, 102, 25
Caffau, E., Ludwig, H. G., Steffen, M., Freytag, B., & Bonifacio, P. 2011, Sol. Phys., 268, 255
Cantat-Gaudin, T., Jordi, C., Vallenari, A., et al. 2018, A&A, 618, A93
Casamiquela, L., Soubiran, C., Jofré, P., et al. 2021, A&A, 652, A25
Cassisi, S., Salaris, M., & Bono, G. 2002, ApJ, 565, 1231
Catalán, S., Isern, J., García-Berro, E., & Ribas, I. 2008, MNRAS, 387, 1693
Chaboyer, B. & Zahn, J. P. 1992, A&A, 253, 173
Chen, Y., Bressan, A., Girardi, L., et al. 2015, MNRAS, 452, 1068
Chen, Y., Girardi, L., Bressan, A., et al. 2014, MNRAS, 444, 2525
Chen, Y., Girardi, L., Fu, X., et al. 2019, A&A, 632, A105
Chieffi, A. & Limongi, M. 2013a, ApJ, 764, 21
Chieffi, A. & Limongi, M. 2013b, ApJ, 764, 21
Chieffi, A. & Limongi, M. 2017, ApJ, 836, 79
Choi, J., Dotter, A., Conroy, C., et al. 2016, ApJ, 823, 102
Christensen-Dalsgaard, J., Monteiro, M. J. P. F. G., Rempel, M., & Thompson, M. J. 2011, MNRAS, 414, 1158
Claret, A. & Torres, G. 2016, A&A, 592, A15
Claret, A. & Torres, G. 2017, ApJ, 849, 18
Claret, A. & Torres, G. 2018, ApJ, 859, 100
Claret, A. & Torres, G. 2019, ApJ, 876, 134
Costa, G., Ballone, A., Mapelli, M., & Bressan, A. 2022, arXiv e-prints, arXiv:2204.03492
Costa, G., Bressan, A., Mapelli, M., et al. 2021, MNRAS, 501, 4514
Costa, G., Girardi, L., Bressan, A., et al. 2019a, A&A, 631, A128
Costa, G., Girardi, L., Bressan, A., et al. 2019b, MNRAS, 485, 4641
Cranmer, S. R. & Saar, S. H. 2011, ApJ, 741, 54
Cranmer, S. R., van Ballegoijen, A. A., & Edgar, R. J. 2007, ApJS, 171, 520
D'Antona, F., Milone, A. P., Tailo, M., et al. 2017, Nature Astronomy, 1, 0186
de Jager, C., Nieuwenhuijzen, H., & van der Hucht, K. A. 1988, A&AS, 72, 259

- Demarque, P., Woo, J.-H., Kim, Y.-C., & Yi, S. K. 2004, *ApJS*, 155, 667
- Dupree, A. K., Dotter, A., Johnson, C. I., et al. 2017, *ApJ*, 846, L1
- Eggenberger, P., Miglio, A., Montalbán, J., et al. 2010, *A&A*, 509, A72
- Ekström, S., Georgy, C., Eggenberger, P., et al. 2012, *A&A*, 537, A146
- Espinosa Lara, F. & Rieutord, M. 2007, *A&A*, 470, 1013
- Evans, D. W., Riello, M., De Angeli, F., et al. 2018, *A&A*, 616, A4
- Fagotto, F., Bressan, A., Bertelli, G., & Chiosi, C. 1994a, *A&AS*, 104, 365
- Fagotto, F., Bressan, A., Bertelli, G., & Chiosi, C. 1994b, *A&AS*, 105, 29
- Freedman, W. L., Madore, B. F., Hatt, D., et al. 2019, *ApJ*, 882, 34
- Freedman, W. L., Madore, B. F., Hoyt, T., et al. 2020, *ApJ*, 891, 57
- Friend, D. B. & Abbott, D. C. 1986, *ApJ*, 311, 701
- Fu, X., Bressan, A., Marigo, P., et al. 2018, *MNRAS*, 476, 496
- Gaia Collaboration, Babusiaux, C., van Leeuwen, F., et al. 2018a, *A&A*, 616, A10
- Gaia Collaboration, Brown, A. G. A., Vallenari, A., et al. 2018b, *A&A*, 616, A1
- Georgy, C., Ekström, S., Eggenberger, P., et al. 2013, *A&A*, 558, A103
- Girardi, L., Bertelli, G., Bressan, A., et al. 2002, *A&A*, 391, 195
- Girardi, L., Bressan, A., Bertelli, G., & Chiosi, C. 2000a, *A&AS*, 141, 371
- Girardi, L., Bressan, A., Bertelli, G., & Chiosi, C. 2000b, *A&AS*, 141, 371
- Girardi, L., Costa, G., Chen, Y., et al. 2019, *MNRAS*, 488, 696
- Girardi, L., Dalcanton, J., Williams, B., et al. 2008, *PASP*, 120, 583
- Girardi, L., Groenewegen, M. A. T., Hatziminaoglou, E., & da Costa, L. 2005, *A&A*, 436, 895
- Godoy-Rivera, D., Pinsonneault, M. H., & Rebull, L. M. 2021, *ApJS*, 257, 46
- Grevesse, N. & Sauval, A. J. 1998, *Space Sci. Rev.*, 85, 161
- Heger, A., Langer, N., & Woosley, S. E. 2000, *ApJ*, 528, 368
- Hidalgo, S. L., Pietrinferni, A., Cassisi, S., et al. 2018, *ApJ*, 856, 125
- Higl, J., Müller, E., & Weiss, A. 2021, *A&A*, 646, A133
- Iglesias, C. A. & Rogers, F. J. 1996, *ApJ*, 464, 943
- Itoh, N., Uchida, S., Sakamoto, Y., Kohyama, Y., & Nozawa, S. 2008, *ApJ*, 677, 495
- Jermyn, A. S., Tout, C. A., & Chitre, S. M. 2018, *MNRAS*, 480, 5427
- Kalirai, J. S., Hansen, B. M. S., Kelson, D. D., et al. 2008, *ApJ*, 676, 594
- Kippenhahn, R., Meyer-Hofmeister, E., & Thomas, H. C. 1970, *A&A*, 5, 155
- Kippenhahn, R. & Thomas, H. C. 1970, in *IAU Colloq. 4: Stellar Rotation*, ed. A. Slettebak, 20
- Kippenhahn, R., Weigert, A., & Weiss, A. 2012, *Stellar Structure and Evolution*
- Komatsu, E., Smith, K. M., Dunkley, J., et al. 2011, *ApJS*, 192, 18
- Lindegren, L., Hernández, J., Bombrun, A., et al. 2018, *A&A*, 616, A2
- Lodders, K., Palme, H., & Gail, H. P. 2009, *Landolt Börnrstein*, 4B, 712
- Maeder, A. 1975, *A&A*, 40, 303
- Maeder, A. 2009, *Physics, Formation and Evolution of Rotating Stars*
- Maeder, A. & Meynet, G. 2000, *A&A*, 361, 159
- Marigo, P. & Aringer, B. 2009, *A&A*, 508, 1539
- Marigo, P., Bressan, A., Nanni, A., Girardi, L., & Pumo, M. L. 2013, *MNRAS*, 434, 488
- Marigo, P., Girardi, L., Bressan, A., et al. 2017, *ApJ*, 835, 77
- McQuillan, A., Mazeh, T., & Aigrain, S. 2014, *ApJS*, 211, 24
- Meynet, G. & Maeder, A. 1997, *A&A*, 321, 465
- Meynet, G., Maeder, A., Schaller, G., Schaerer, D., & Charbonnel, C. 1994, *A&AS*, 103, 97
- Miglio, A., Brogaard, K., Stello, D., et al. 2012, *MNRAS*, 419, 2077
- Mocák, M., Müller, E., Weiss, A., & Kifonidis, K. 2008, *A&A*, 490, 265
- Mowlavi, N., Eggenberger, P., Meynet, G., et al. 2012, *A&A*, 541, A41
- Noll, A., Deheuvels, S., & Ballot, J. 2021, *A&A*, 647, A187
- Paxton, B., Bildsten, L., Dotter, A., et al. 2011, *ApJS*, 192, 3
- Paxton, B., Schwab, J., Bauer, E. B., et al. 2018, *ApJS*, 234, 34
- Pietrinferni, A., Cassisi, S., Salaris, M., & Castelli, F. 2004, *ApJ*, 612, 168
- Pols, O. R., Schröder, K.-P., Hurley, J. R., Tout, C. A., & Eggleton, P. P. 1998, *MNRAS*, 298, 525
- Potter, A. T., Tout, C. A., & Eldridge, J. J. 2012, *MNRAS*, 419, 748
- Reimers, D. 1975, *Memoires of the Societe Royale des Sciences de Liege*, 8, 369
- Reimers, D. 1977, *A&A*, 61, 217
- Renzini, A. & Fusi Pecci, F. 1988, *ARA&A*, 26, 199
- Riello, M., de Angeli, F., Evans, D. W., et al. 2021, *VizieR Online Data Catalog*, J/A+A/649/A3
- Rosenfield, P., Marigo, P., Girardi, L., et al. 2014, *ApJ*, 790, 22
- Roxburgh, I. W. 1978, *A&A*, 65, 281
- Royer, F., Zorec, J., & Gómez, A. E. 2007, *A&A*, 463, 671
- Salaris, M., Serenelli, A., Weiss, A., & Miller Bertolami, M. 2009, *ApJ*, 692, 1013
- Sandquist, E. L., Latham, D. W., Mathieu, R. D., et al. 2021, *AJ*, 161, 59
- Sarajedini, A., Dotter, A., & Kirkpatrick, A. 2009, *ApJ*, 698, 1872
- Saslaw, W. C. & Schwarzschild, M. 1965, *ApJ*, 142, 1468
- Schröder, K. P. & Cuntz, M. 2005, *ApJ*, 630, L73
- Schwarzschild, M. 1958, *Structure and evolution of the stars*. (Princeton, Princeton University Press, 1958.)
- Song, N., Alexeeva, S., Sitnova, T., et al. 2020, *A&A*, 635, A176
- Sonoi, T., Ludwig, H. G., Dupret, M. A., et al. 2019, *A&A*, 621, A84
- Spada, F., Demarque, P., Kim, Y. C., Boyajian, T. S., & Brewer, J. M. 2017, *ApJ*, 838, 161
- Spera, M., Mapelli, M., Giacobbo, N., et al. 2019, *MNRAS*, 485, 889
- Stello, D., Vanderburg, A., Casagrande, L., et al. 2016, *ApJ*, 832, 133
- Talon, S. & Zahn, J. P. 1997, *A&A*, 317, 749
- Tang, J., Bressan, A., Rosenfield, P., et al. 2014, *MNRAS*, 445, 4287
- Torres, G., Vaz, L. P. R., Sandberg Lacy, C. H., & Claret, A. 2014, *AJ*, 147, 36
- Ventura, P., Zeppieri, A., Mazzitelli, I., & D'Antona, F. 1998, *A&A*, 334, 953
- Viani, L. S., Basu, S., Ong J., M. J., Bonaca, A., & Chaplin, W. J. 2018, *ApJ*, 858, 28
- Vink, J. S., de Koter, A., & Lamers, H. J. G. L. M. 2001, *A&A*, 369, 574
- Viscasillas Vázquez, C., Magrini, L., Casali, G., et al. 2022, *A&A*, 660, A135
- von Steiger, R. & Zurbuchen, T. H. 2016, *ApJ*, 816, 13
- von Zeipel, H. 1924a, *MNRAS*, 84, 665
- von Zeipel, H. 1924b, *MNRAS*, 84, 684
- Weiss, A. & Schlattl, H. 2008, *Ap&SS*, 316, 99
- Xu, Y., Goriely, S., Jorissen, A., Chen, G. L., & Arnould, M. 2013, *A&A*, 549, A106
- Zahn, J. P. 1992, *A&A*, 265, 115